Article

Not peer-reviewed version

The Diversity of Crystals, Microstructures and Texture That Form Ostreoidea Shells

Anna Sancho Vaquer , Erika Griesshaber , Carmen Salas , Elizabeth M. Harper , Antonio G. Checa * , Wolfgang W. Schmahl

Posted Date: 3 February 2025

doi: 10.20944/preprints202502.0108.v1

Keywords: microstructure of oyster shells; texture of oyster shells; high-resolution EBSD; misorientation between crystals; turbostratic texture; crystal twin formation

 doi:10.20944/preprints202502.0108.v1

Article

The Diversity of Crystals, Microstructures and Texture that Form Ostreoidea Shells

Anna Sancho Vaquer [1], Erika Griesshaber [1], Carmen Salas Casanova [2], Elisabeth M. Harper [3], Antonio G. Checa [4] and Wolfgang W. Schmahl [1]

[1] Department of Geo- and Environmental Sciences, Ludwig-Maximilians-Universität München, Munich, 80333, Germany

[2] Departamento de Biología Animal, Facultad de Ciencias, Universidad de Málaga, Málaga, 29010, Spain

[3] Department of Earth Sciences, University of Cambridge, Cambridge, CB2 3EQ, UK

[4] Departamento de Estratigrafía y Paleontología, Universidad de Granada, Granada, 18071, Spain

* Correspondence: acheca@ugr.es

Abstract: The shell of Ostreoidea is specific among that of bivalves, as it comprises many crystal microstructures and crystal textures. This stems from the fact that into the basic shell structure, consisting of columnar, foliated, granular calcite and myostracal aragonite, voids are incorporated: the pores of the vesicular segments and the blades/laths of the chalk lenses. Furthermore, cementation to uneven-surfaced substrate requires the formation of corrugated shell morphologies and adjustments of crystal organization for the generation of convex/concave shell surfaces. We investigated the shell of *Magallana gigas*, *Ostrea stentina*, *Ostrea edulis* (Ostreidae) and *Hyotissa hyotis*, *Hyotissa mcgintyi*, *Neopycnodonte cochlear* (Gryphaeidae) with high-resolution, low-kV, electron backscatter diffraction (EBSD) measurements and scanning electron microscopy (FE-SEM) imaging. From a crystallographic perspective we, (i) characterized the sub-micrometer crystal assembly of ostreoid microstructures and textures, (ii) investigated crystal organization at the changeover from one microstructure into the other, and (iii) examined how curved crystal surfaces are generated at inner shell surface and within the shell, in and at aggregations of folia. We show that Ostreoidea are capable to secrete, within the same shell, single crystalline, graded and polycrystalline calcite, the latter with almost random orientation. We demonstrate that Ostreoidea myostracal aragonite is twinned, while Ostreoidea calcite is not twinned, neither the calcite within the different microstructures, nor the calcite at the changeover from one microstructure into the other. We highlight the very specific microstructure of the foliated shell and demonstrate the strongly regulated gradedness of both, the c- and a*-axes orientation of the foliated calcite crystallites.

Keywords: microstructure of oyster shells; texture of oyster shells; high-resolution EBSD; misorientation between crystals; turbostratic texture; crystal twin formation

1. Introduction

Ostreoidea appeared in the Triassic and comprise a superfamily with a long paleontological record [1–3]. Ostreoidea evolved into ecologically very successful marine organisms and have today a global distribution across a wide range of salinities and habitats [4,5]. Ostreoidea colonize intertidal to subtidal, marine to brackish environments [3,6]; nonetheless, some species (*Neopycnodonte zibrowii* Gofas, Salas and Taviani 2009) extend into deep water, up to about 2000 m water depths [6,7].

The shells of Ostreoidea are composites of biopolymers and minerals (e.g. [3,8–12]). The biopolymer component is present in the shell (i) as a network between the crystallites, (ii) as thick membranes encasing the columns, (iii) as an organic glue surrounding the cementation granules and, only for the *Ostrea* sp., (iv) as an organic layer incorporating an assembly of rhombohedral crystals [13].

 doi:10.20944/preprints202502.0108.v1

The superfamily of Ostreoidea comprises the families Gryphaeidae (foam oysters) and Ostreidae (true oysters) [12,14,15]. Species of both families form their shell of low-Mg calcite and myostracal and ligament aragonite [16–18]. In this regard, the Ostreoidea are specific among bivalves. While species of many bivalve families secrete for shell formation aragonite or superimposed layers of aragonite and calcite, Ostreoidea use calcite for shell generation, disregarding the myostracal and ligament aragonite [3,19].

Below an outermost thin organic periostracum [17], Ostreoidea secrete six Ca-carbonate microstructures. The bulk of the Ostreoidea shell consists of foliated calcite (e.g. [16–22]), complemented, however, along the external surface of both valves, though particularly the right one, with a seam of columnar calcite [16,23,24], and, along sections of the proximal surface of the lower valve, with a cementation layer comprising granular calcite [4,25–27]. The muscle attachment sites, myostraca, are formed of prismatic aragonite. The columnar, foliated, granular calcite and myostracal, prismatic, aragonite microstructures generate compact shell layers. However, Ostreoidea incorporate voids into their shell; a further structural characteristic that is specific for these bivalves. Ostreidae incorporate large volumes of a meshwork of wavy calcite blades and laths into the foliated shell, forming the chalk lenses [17,19,28]. Gryphaeidae incorporate lenses of submicrometer- to micrometer-sized pores within the foliated shell [13].

The Ostreoidea have life spans of about 10 years, up to a maximum of 20 years. Nonetheless, they form thick shells within a few years [29]. This can be achieved by incorporating large volumes of cavities into the structural material of the shell; a unique strategy developed, among bivalves, only by the Ostreoidea for producing in short time thick and robust shells [30]. The chalk and the vesicular lenses have irregular extensions and varying thicknesses within the shells. In shell cross-sections, the growth lines are widely spaced between the foliated layer and the chalk or between the foliated layer and the vesicular microstructure. This indicates a higher thickening speed for the cavity-rich microstructures, relative to the speed of thickening of the foliated material [12,22]. In addition, it is also demonstrated that the chalk assists with its cavity-rich structural plasticity the attachment of the oyster shell to uneven-surfaced substrates (e.g. [31] and references therein).

In the study presented here we summarize and review crystallographic aspects for all types of crystals and crystal units that we observe, so far, for Ostreoidea shells. The latter are ideal for understanding the morphological, crystallographic and organizational diversity of biologically secreted Ca-carbonate crystals, as the compact Ostreoidea shell layers comprise not only the five main microstructures (columnar, foliated, granular, prismatic (the myostraca) and rhombohedral (the latter the Ostreidae only)), but also the cavity-rich assemblies of the chalk blades and laths in the Ostreidae and the fractal-shaped dendritic polyhedral crystals, surrounding the vesicular pores in the Gryphaeidae. In addition, due to this huge diversity in crystal shapes, types and organizational patterns, Ostreoidea shells are best suited for examining the crystallographic nature at the changeover from one microstructure into the other. We find five transitions between adjacent crystal assembly patterns. Disregarding the aragonite of the myostraca, all Ostreoidea shell microstructures are formed of only one Ca-carbonate polymorph, calcite, hence, there is no delimitation between adjacent microstructures in form of, e.g. a biopolymer membrane, as it is often the case when the shell is formed of superimposed layers of calcite and aragonite [32]. Accordingly, the changeover from one microstructure into the other is, to a large degree, controlled for Ostreoidea shells by crystallographic aspects of the relevant crystals and microstructures.

The foliated shell layer with its specific microstructure and outstanding texture is topologically related to all other shell microstructures. Accordingly, for understanding the shell as a structural entity, one major aim of this study, it is essential to assess the crystallographic-structural attributes of all types of shell-forming crystals and crystal units as well as of the microstructures these generate. Crystallographic characteristics of crystals and their assemblies are best characterized with diffraction methods, X-ray diffraction or electron backscatter diffraction (EBSD) carried out with a scanning electron microscope (SEM) or a transmission electron microscope (TEM). The advantage of X-ray diffraction analysis for structure determination is that the measurement covers a large section

 doi:10.20944/preprints202502.0108.v1

of the sample [21,24,32,33], however, it determines the texture of the material and does not render its microstructural characteristics. Electron backscatter diffraction measures and visualizes both the microstructure and the texture of the material in question, nonetheless, high-resolution individual EBSD scans cover small sample portions, relative to sample sections that can be examined with XRD measurements. However, the advantage of EBD measurements is that, in addition to texture determination, many crystallographic attributes, e.g. the mode and degree of misorientation between crystals, crystal morphology, degree of interlinkage and many more are obtained. These can be related to the observed texture patterns and, even though, in general, smaller sample sections are scanned, the mode of crystal organization can be better assessed and understood. In addition, EBSD measurements render very local, very small-scaled, crystallographic-structural attributes as well, in comparison to what is obtained with XRD measurements.

When EBSD is carried out conventionally with an SEM-EBSD system, an acceleration voltage of 20 kV is used. This gives a minimal space resolution between 300 and 400 nm. The foliated calcite of Ostreoidea shells consists of parallel arrays of 200 to 400 nm thick, 2-4 μm wide and up to 20 μm long folia (e.g. this study and [20,21,28]). The columnar, granular, blade/laths-shaped, fractal-dendritic and prismatic crystals are topologically related to the foliated shell. Hence, for high-quality EBSD measurements, as it is required for the crystallographic characterization of the foliated, granular and chalk structures, EBSD data acquisition must be conducted with a space resolution of 100 to 200 nm. A space resolution of 300-400 nm is not fine scaled enough for deciphering on the nm range crystallographic and structural aspects of the crystals.

We performed for this study low kV electron backscatter diffraction (EBSD) measurements on adult Ostreidae and Gryphaeidae shells. Measurements were conducted with an acceleration voltage below 20 kV, down to very few kV's, as described for biological carbonates [34]. This renders a space resolution, depending on the used kV, of 100 to 200 nm. We performed for this study EBSD measurements at 15, 12, even at 8 kV and investigated shell crystal microstructure and texture for: the Ostreidae *Magallana gigas* (Thunberg, 1793), *Ostrea stentina* Payraudeau, 1826, *Ostrea edulis* Linnaeus, 1758 and the Gryphaeidae *Hyotissa hyotis* (Linnaeus, 1758), *Hyotissa mcgintyi* (H. W. Harry, 1985) and *Neopycnodonte cochlear* (Poli, 1795). EBSD results were complemented with FE-SEM micrographs, taken on fractured surfaces. As our study is conducted on very small-scale levels, we wanted to ensure that the structural information is not distorted by etching artefacts, hence, we did not image etched shell surfaces.

The following questions led to the present study:

1. Do we find a comparable diversity in crystal texture in Ostreidae shells, as observed for the microstructures?
2. How are crystallographic axes of crystals organized at the transition between adjacent microstructures? Is there continuity or discontinuity in crystallographic axes orientation between adjacent microstructures?
3. How are the round surfaces of the pores accomplished within the shells?
4. How is a convex and concave shell surface generated with foliated crystal units?
5. How can we address the nature of the foliated shell layer texture?

Accordingly, subsequently, we characterize the nanometer scale internal structure of the shell forming crystals and crystal units, address their microstructure, address their texture and describe the degree and mode of misorientation between the crystals and the crystal units. Based on results gained from the latter we demonstrate (i) crystallographic axes discontinuity and some continuity between adjacent microstructures, (ii) the mode of crystallographic axes organization at the change from one microstructure into the other and (iii) discuss possible determinants for the changeover from one shell structure into the other, such as crystal twinning, gradation in crystal orientation or oriented nucleation. (v) We address the very specific texture of the foliated shell layer and discuss for the latter possible texture modes, such as: an axial texture, a turbostratic texture or a spherulitic texture. (v) We illustrate, from a structural point of view, the accomplishment of curvature within the shells as well as at shell inner surface.

 doi:10.20944/preprints202502.0108.v1

Sample preparation for FE-SEM imaging and EBSD measurements

The shells were cut transversely. Shell pieces were embedded into epoxy resin and several mechanical grinding and polishing steps were performed on them. The final polishing, consisting of etch-polishing with colloidal alumina, with ~0.06 μm particle size, was performed using a vibratory polisher. EBSD measurements required 4-6 nm of carbon coating, while for FE-SEM imaging samples were coated with 5 nm Pt/Pd.

EBSD measurements and data analysis

A Hitachi SU5000 field emission SEM, equipped with an Oxford Instruments Nordlys II EBSD detector, was used to perform the measurements. The SEM operation during measurements was mainly at 12 and 15 kV, for some measurements at 8 kV. We discuss six Ostreoidea species. In order to understand the structure of the shell well, we performed 12 to 14 EBSD measurements per species.

For Kikuchi indexing, the Oxford Instruments CHANNEL 5 and AZTec Crystal software were used. Most measurements were done with increments of 100 to 200 nm, for none of the measurements was the step size higher than 300 nm. This ensured very high indexing rates, over 95%. The latter is necessary for understanding the foliated calcite arrangements and the nature of the transitions from one microstructure into the other.

Terminology

This study uses the terms: crystallites, crystals, crystal units, mesocrystals, assemblies of crystallites and assemblies of crystals.

The *idealized concept* of a *crystal* or of a *crystallite* refers to a structure in which matter is arranged in a perfectly regular, periodically repeating spatial pattern. The latter is the crystal lattice, which extends coherently in all directions over the space occupied by the crystal.

For the crystals discussed in this study, the crystal lattice is 3-dimensional. *Real crystals* develop during their growth, imperfections, e.g. incorporate impurities, adopt dislocations. Due to these *real crystals* implement *small-angle grain boundaries*, e.g. at arrays of dislocations and at these boundaries the crystal lattice takes a slightly different orientation [35]. Accordingly, *real crystals* consist of subunits and these are tilted to each other by a small angle, for which an upper limit of 10° is often used [35]. These subunits are termed mosaic blocks or mosaic domains.

We regard the foliated units to be *mesocrystals*. A mesocrystal is defined as a mesoscopically structured crystal, consisting of submicrometer-sized crystallites and organized within the mesocrystal with a good crystallographic register. Nonetheless, the crystallites in mesocrystals are separated from each other by voids and/or impurities [36–38].

We use in this study the term *crystal unit* for morphological mosaic- or mesocrystal entities such as columns, prisms, blades, laths, rhombohedra, polyhedra or granules. These crystal units assemble in the shell of the investigated species to microstructures. These have different modes of preferred crystallographic orientation or crystal textures.

Shell microstructures are presented in this study with EBSD band contrast measurement and crystal orientation maps. EBSD band contrast is shown grey-scaled, crystal orientation in the maps are shown color-coded. We use the inverse pole figure (IPF) and all-Euler colouring codes. The relevant coloring-code is either given in the figure or indicated in the figure caption.

Crystal texture or the *crystallographic preferred orientation of crystals or crystal units* is shown with pole figures. These display either crystal orientation data or their density distribution. The density distributions that we show in this study are calculated with a half-width of 5° and a cluster size of 3°. The half-width gives the spread of the poles over the surface of the projection sphere. The cluster with a chosen size gives information on the amount of poles that have the same orientation.

We discuss in this contribution different carbonate *crystal textures*.

 doi:10.20944/preprints202502.0108.v1

A *single-crystal-like crystal textures* is present when we observe in the pole figure one cluster for c-axes and clusters as well for either the three a*-axes of the calcite or the a- and b-axes of the aragonite.

A *single-crystal-like texture with a graded distribution of calcite c- and a*-axes* is given when we find in the pole figures individual clusters for the crystallographic axes orientations, however, the clusters display a longish appearance, due to the recurrent gradual tilt of crystallographic axes distribution for each cluster.

An *axial crystal textures* is given when we observe clustering in c-axes orientation, however, scattering of the corresponding a*-axes (calcite) or a- and b-axes (aragonite) orientations on a great circle perpendicular to the texture axis, here the c-axis, direction.

Crystal co-orientation strength is calculated from the density distribution of EBSD orientation data and is given either for entire EBSD scans or the subsets of these. Crystal co-orientation strength is presented with *MUD (multiple of uniform (random) distribution) values.* A high MUD indicates a high crystal co-orientation strength, a low MUD indicates low or no crystal co-orientation strength. If, at a half-width of 5° and a cluster size of 3°, the MUD value is below 3, the orientation data have a random distribution or lack preferred crystal orientation. If, at a half-width of 5° and a cluster size of 3°, the MUD values are higher than 700, this indicates a very high, single-crystal-like, crystal co-orientation.

The degree of tilt or *misorientation between crystallites and crystals* is obtained from EBSD measurements. We show misorientation between crystals with (i) relative frequency-misorientation angle or (ii) misorientation angle-distance diagrams. The misorientation-distance diagrams are given for trajectories a to b, c to d. The chosen trajectories run either parallel to the length of a foliated unit or perpendicular to the length of a foliated unit. For the misorientation angle-distance diagrams we give either the cumulative misorientation angle, thus, the cumulative increase in misorientation relative to the first point on the trajectory, or we give the local misorientation, misorientation from point to point along the trajectory, hence, misorientation from crystallite to crystallite along the trajectory.

2. Results

EBSD band contrast measurement maps of Figure 1 highlight the different microstructures that were observed for the investigated Ostreoidea shells. As the crystal assembly patterns are not only characterized by crystal or/and crystal unit shape, size, structure and organization, but also by the degree and mode of misorientation between the constituting crystals, we highlight for the different modes of crystal organization the corresponding pattern of misorientation between the crystals (Figs. 1, 2). For the investigated Ostreoidea species we find an ordered as well as a disordered pattern of misorientation between the comprising crystals (Fig. 2). For discrimination between ordered and disordered misorientation patterns, we show the MacKenzie curves for calcite and aragonite. These give the distribution of misorientation angles for randomly textured carbonate polycrystals (Fig. 2H, [39]).

 doi:10.20944/preprints202502.0108.v1

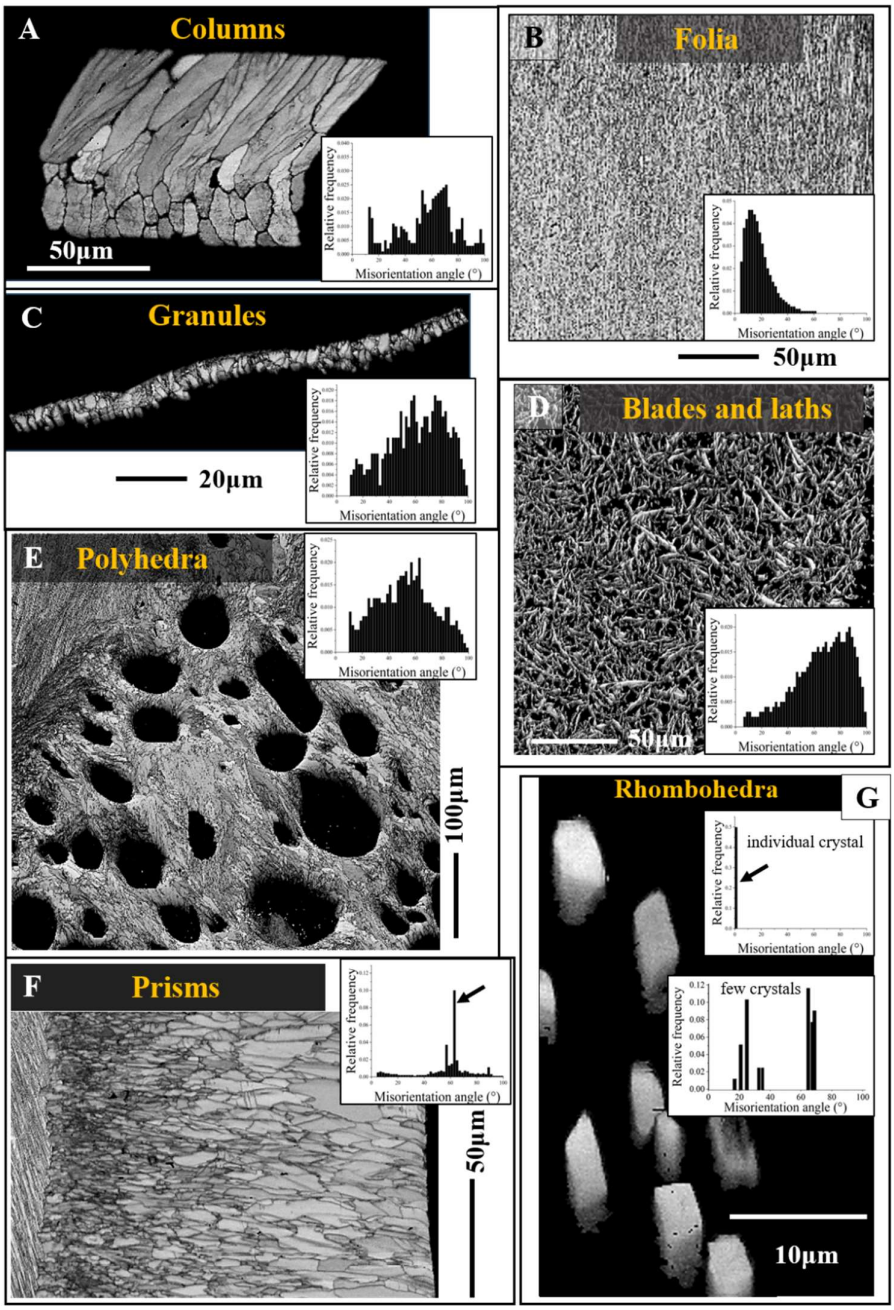

Figure 1. Ostreoidea shell crystal morphology, shell layer internal structuring and relative frequency-misorientation angle distributions for the different crystal assembly patterns. A to G: EBSD band contrast measurement images. The inserts give relative frequency versus misorientation angle diagrams for the shown EBSD scans and, thus, microstructures. A: Sequence of columns seaming outer valve surfaces. B: Array of folia forming the foliated units. C: String of granules intercalated into the organic matrix of the cementation layer, the layer that attaches the lower valve external surface to the substrate. D: Meshwork of blades and laths forming the cavity-rich structure of the chalk. E: Conglomeration of variously sized dendritic, polyhedral crystals facilitating the occlusion of pores into the Gryphaeidae shells. F: The prisms of the myostraca, the shell section where the muscles attach to. G: Accumulation of rhombohedral crystals within organic substance in Ostreidae shells.

 doi:10.20944/preprints202502.0108.v1

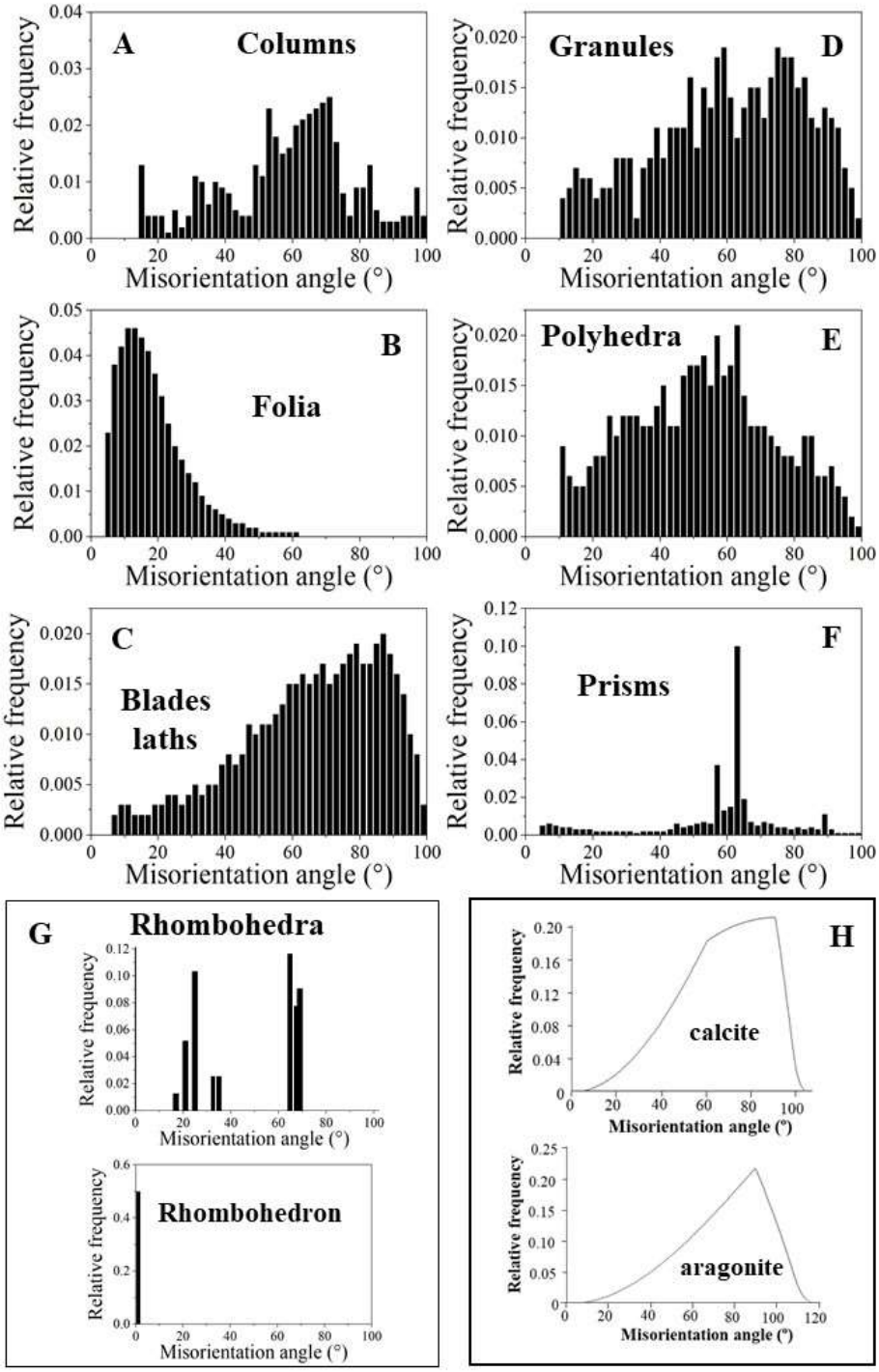

Figure 2. Diversity in relative frequency-misorientation angle patterns for the microstructures that comprise Ostreoidea shells (A to G). H: MacKenzie curves for random misorientation angle distribution [40], given for calcite and aragonite. A, C, D, E: Random distribution of misorientation angles. B, F, G: Structured distribution of misorientation angles, note the structured distribution of misorientation angles for folia (B). We find for (A) and (E) a comparable pattern for the distribution of misorientation angles, alike for (C) and (D). For the latter, we find a gradual change and increasing development to the formation of large misorientations. Note the difference in magnitude of misorientation angle between the assembly of folia (B) and the assembly of chalk blades/laths (C).

 doi:10.20944/preprints202502.0108.v1

We observe significant structural differences for the crystals that comprise the microstructures of the investigated Ostreoidea shells. Columnar prisms are graded in size towards the outer shell surface (Figs. 1A, S1). Individual columns are markedly structured (Figs. 1A, S1); however, the comparison of the band contrast maps and the misorientation angle patterns shows that the structuring within the columns is not resembling the internal structuring of the foliated units (Figs. 1A, B, S1). For the latter, well visible from the band contrast map is the, more or less, parallel arrangement of folia (Fig. 1B). This is not observed for the internal architecture of the columns. The layer that cements the outer surface of the lower valve comprises a conglomerate of granules and small prism-shaped crystals (Fig. 1C). The microstructure of the chalk is a meshwork of interlaced, in part, connected calcite blades and laths, where the latter often have curved/undulated morphologies (Fig. 1D). The occlusion of vesicular pores into the shell is accomplished with the generation of a shell layer microstructure consisting of a tight interlinkage of variously sized, strongly fractal-shaped, polycrystals (Fig. 1E). These form a dense microstructure and encase the round-shaped pores (Fig. 1E). The microstructure of adductor and pallial myostraca (the muscle attachment sites) results from an interconnection of aragonite prisms (Fig. 1F). The prisms are graded in size and increase in dimension towards the inner shell surface (Fig. 1F). Most striking and only observed for the Ostreidae is the formation of crystals with strictly rhombohedral morphologies (Fig. 1G). The morphology of these crystals is distinct to that of other biologically secreted Ca-carbonate crystals and resemble inorganic rhombohedra precipitated from solution [41,42]. A detailed description of the rhombohedron-shaped crystals is given by Sancho Vaquer et al. (2025) [13]. Accordingly, we not only find significant differences in morphologic-structural attributes of crystal, crystal unit and shell layer microstructures, but also in the corresponding misorientations between the microstructures comprising crystals (Fig. 2). For the columns (Fig. 2A), the granules (Fig. 2D), the dendritic crystals (Fig. 2E) and the chalk blades/laths we observe a wide range in misorientation angle, up to 100°, and a misorientation angle distribution that equals random distribution (see the MacKenzie curves in Fig. 2H). Random distribution of misorientation angles is not observed for the assembly of folia (Fig. 2B), for the rhombohedral crystals (Fig. 2G and [13]) and for the assembly of myostracal prisms (Fig. 2F). The misorientation angle distribution of myostracal prisms is specific. We find a large range in misorientation angle distribution (Fig. 2F), however, the myostracal crystal misorientation diagram is dominated by a marked peak at 64° misorientation (Fig. 2F). Note also the difference in the degree of misorientation angle between the assembly of foliated crystals (Fig. 2B) and the assembly of chalk blades/laths (Fig. 2C). For the foliated crystals we see a large peak at low-angle misorientations, while for the chalk blades, we see a large peak mainly at large-angle misorientations.

Subsequently, we present in more detail the structural and crystallographic attributes of the crystals and crystal units that form the different shell layers of the investigated Ostreoidea species (Figs. 3 to 14, S1 to S5).

Calcite columns with dimensions of 8-10 mm x 4-5 mm x 40-50 mm (e.g., for *M. gigas*) seam large sections of the distal, outer, surface of the two valves (Fig. 3A). BSE images show an internal layering of individual columns, consisting of equally sized dark and light bands (Fig. 3B, C). These reflect differences in organic content (light layers are more mineralized, the dark bands are more organic-rich) and indicate different stages of column growth. The internal structure of the columns is specific (Figs. 3D, E, F, S2, S3). We observe in the band contrast measurement images that the columns consist of subunits or domains (Figs. 3E, F, S3). These are formed of platy crystals (Fig. S3C), nonetheless, the width, length and morphology of these platy crystals do not resemble at all those of the folia which form the foliated units of the foliated shell (compare images of Figs. S3A to C with images shown in Fig. 4A to C). The columnar subunits (domains) consist of thin, platy, irregularly shaped crystallites, resembling flakes. Nonetheless, as it is the case for the folia in foliated units, the crystallites within a columnar subunit are strongly co-oriented; misorientation within the columnar subunits/domains is low, it scatters up to about 5°. Even though the calcite of individual columns is well co-oriented, columnar calcite cannot be addressed as being single crystalline (Fig. 3J, K). Contrasting to the latter,

 doi:10.20944/preprints202502.0108.v1

the calcite of arrays of columns is very little co-oriented (see MUD value in Fig. 3I), a characteristic that resembles the arrangement of folia in foliated crystals and that of foliated crystals in the foliated shell layer (see MUD value in Fig. 3H). We find for the investigated Ostreoidea shells that within the individual crystals or crystal units (a column or a foliated unit) the crystallites are very well co-oriented, however, for the assembly of these crystals/crystal units we find very low crystal co-orientation strength. The texture pattern of individual columns is single-crystal-like (pole figure in Fig. 3J), while the texture pattern of an assembly of columns is axial (pole figure in Fig. 3I).

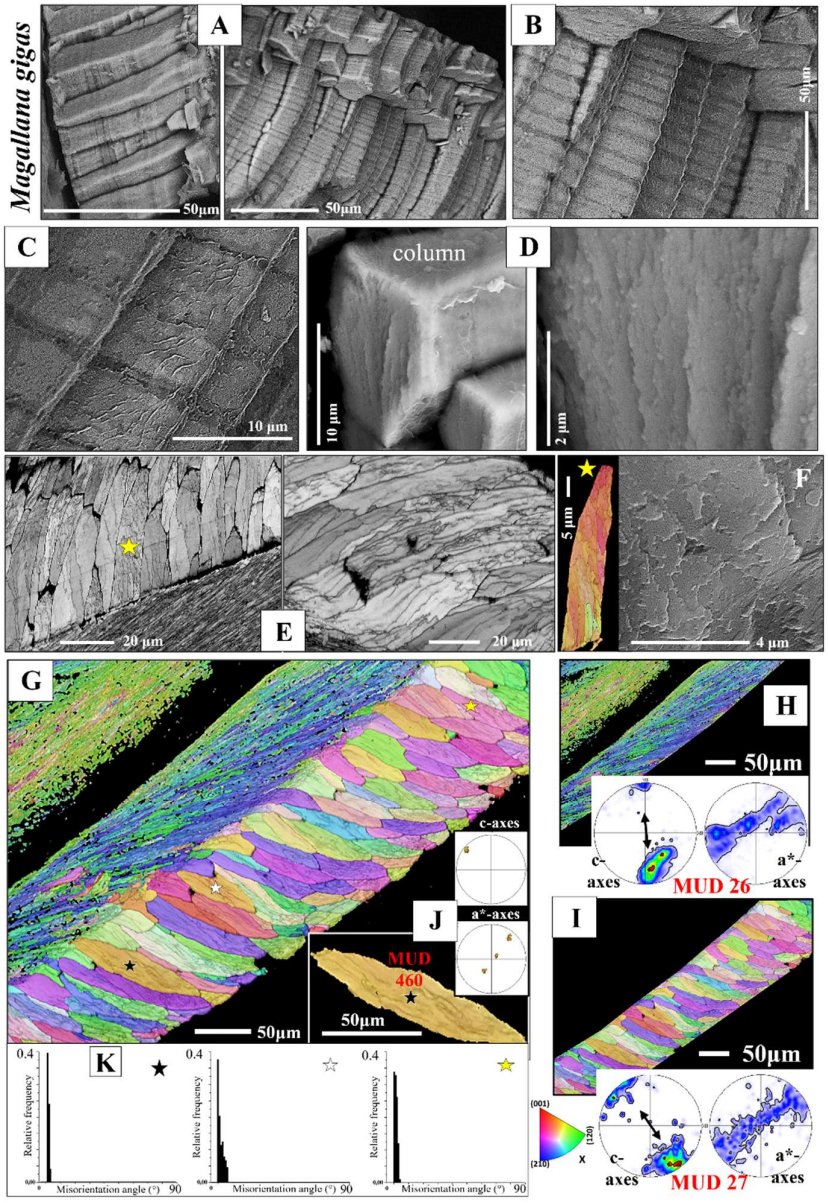

Figure 3. Internal structure, microstructure, crystal texture and crystal co-orientation strength of the array of columns that seam the outermost valve layer of *Magallana gigas* shells. A to D, F: BSE micrographs. E: EBSD band contrast measurement image. F, G, I, J, K: Color-coded crystal orientation (EBSD maps), crystal texture (pole figures) and crystal co-orientation strength (MUD value) of individual columns (J, K, L) and of arrays of columns (G, I). H: The foliated shell adjacent to a sequence of columns (I). Note the difference in texture but similarity in crystal co-orientation strength for the columns and for the adjacent sequence of foliated units (H, I). Individual columns are internally structured and are formed of subunits (domains) consisting of well co-oriented calcite crystallites (F, J) (Fig. S3B). The internal structure of the columns as well as of their subunits is different to that

 doi:10.20944/preprints202502.0108.v1

of the foliated units, nonetheless, we find only low angle misorientations within the columns (see the relative frequency-misorientation angle diagrams for individual columns in (K)), as it is also the case for the assembly of folia and foliated units (see the misorientation angle diagram in Fig. 1B). Note the layering within the columns (A to C), visualizing different growth stages. Black arrows in the pole figures in (H) and (I) indicate the overall direction of c-axis orientation and show an about 30° misorientation in c-axis orientation between an array of columns and the adjacent foliated shell (H, I). At EBSD data acquisition and EBSD data evaluation, the three Euler angles were kept at 0°; $\phi1$=0°, Φ=0°, $\phi2$=0°.

Structural properties and crystallographic attributes of units forming the foliated shell layer are presented with Figs. 4-9, S4. BSE images of Fig. 4A, C visualize the thickness and width of individual folia, while Fig. 4B shows the shape and size of crystals that comprise a folium. A folium is formed of, more or less, parallel arrays of lath-shaped crystals with arrowhead endings (Fig. 4B and [20]). The calcite of individual folia is very co-oriented (MUD values 591, 626, Fig. 4D). It can be addressed to be single crystal like, as EBSD measurements show that individual folia have a single-crystal-like long-range crystallographic order (see pole figures in Fig. 4D).

 doi:10.20944/preprints202502.0108.v1

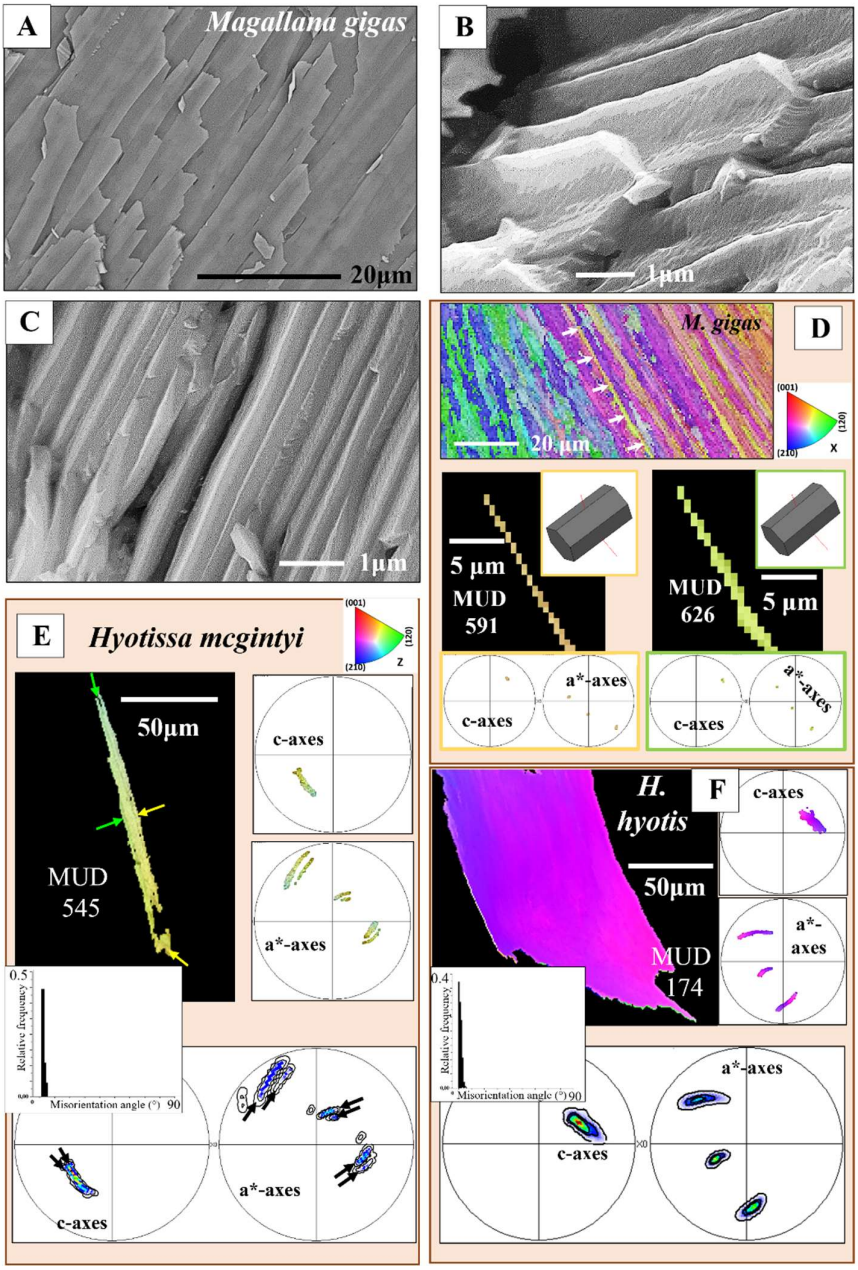

Figure 4. The folia and assemblies of folia that generate ostreoidean foliated units, e.g., as those shown in E and F. A to C: BSE micrographs highlighting the morphology and dimension (width and thickness) of lath-shaped, arrowhead ended crystals and of individual folia. D: Crystal orientation, crystal texture and crystal co-orientation strength of two individual folia. The calcite of a folium is strongly co-oriented (see MUD values in D). E, F: EBSD scans of foliated units, consisting of stacks of folia. Note the mode of c- and a*-axes orientation distribution in the pole figures (E, F). The gradual change in color (EBSD map and pole figures), as well as the gradual change in tilt of both crystallographic axes (see the pole figures), demonstrates that the foliated crystal units are entities with a graded calcite c- and a*-axes orientation. We observe a marked gradedness in orientation for both, calcite c- as well as a*-axes. E, F: Relative frequency-misorientation angle diagrams are given for the crystal shown in the figure; we observe very low misorientation angles between adjacent folia. Euler angles were kept at zero for EBSD data acquisition and analysis for the measurements shown in D, E, F.

When investigating calcite c- and a*-axes orientation of a stack of folia, generating a foliated unit (e.g., Fig. 4E, F), we observe an elongated appearance of the c- and a*-axes orientation data points in

 doi:10.20944/preprints202502.0108.v1

the pole figure. This is an expression of the gradation in calcite c- and a*-axes orientation (see pole figures in Fig. 4E, F); it is the result of a graded assembly of folia in the foliated unit (Figs. 5). Gradation of one of the crystallographic axes of calcite or aragonite crystals is observed for biological carbonates, however, gradation in all crystallographic axes of carbonate crystals is outstanding. For biologically secreted calcite, this study is the second report so far that demonstrates the gradation of both the c- as well as the a*-axis of the calcite in a crystal unit.

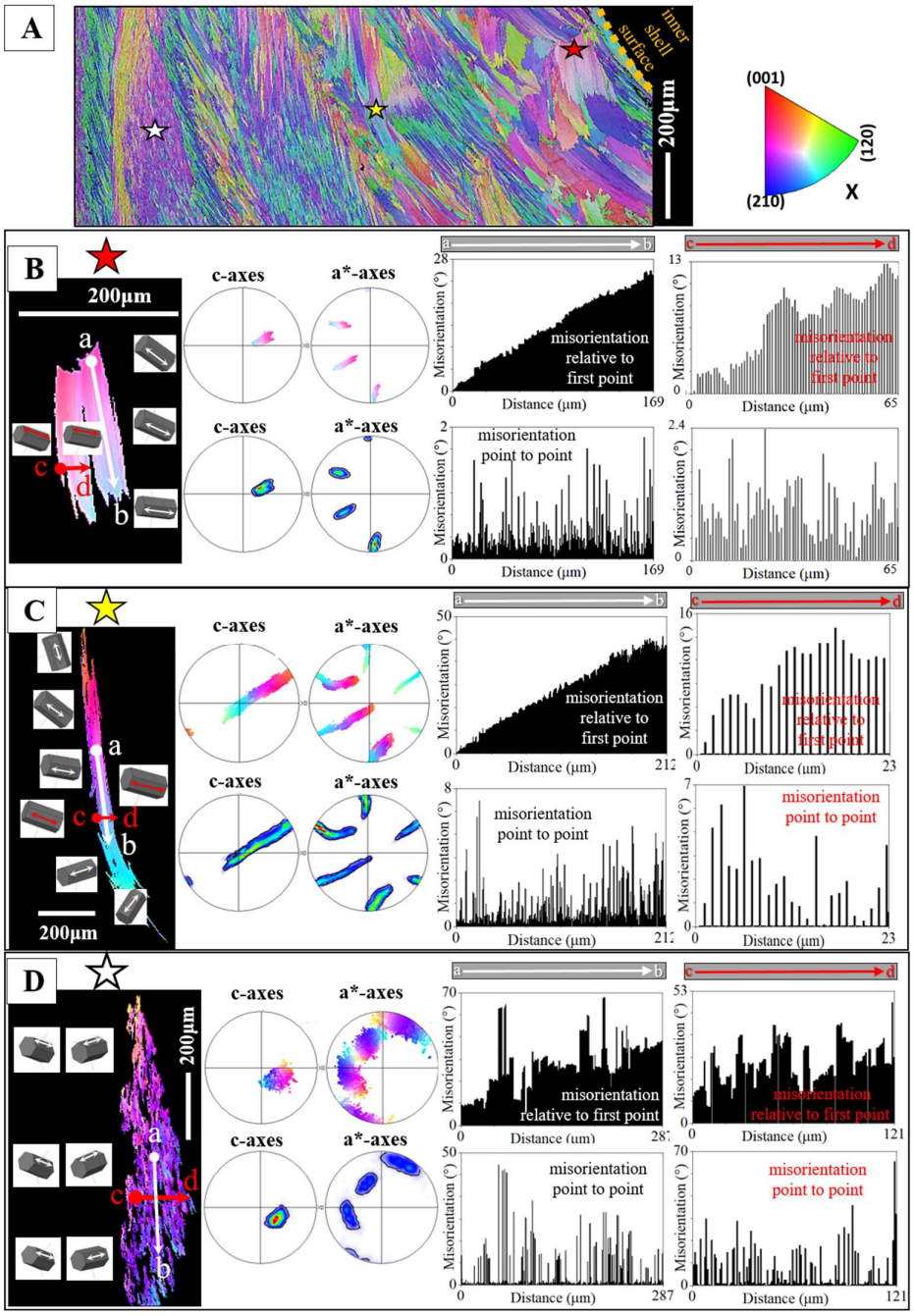

Figure 5. A: EBSD crystal orientation map of an assembly of foliated crystals for the shell of *Hyotissa hyotis*, visualizing their size, internal structure and interlinkage. B to D: Individual foliated units selected from different parts of the foliated shell (indicated with a red, yellow or white star in the EBSD map in (A)). The organization of crystallographic c- and a*-axes of/in the foliated units is indicated with sketched crystals and corresponding

 doi:10.20944/preprints202502.0108.v1

misorientation angle - distance diagrams. These show misorientation between crystallites along trajectories a to b and c to d (B to D). We give (i) the cumulative misorientation angle, the increase in misorientation angle, relative to the first point on the trajectory and (ii) the misorientation angle from point to point along the trajectory, thus the local misorientation angle, misorientation between adjacent crystals. For the foliated units shown in (B) and (C), we observe a gradual rotation of crystallographic c- and a*-axes orientation, in both directions, along the length as well as perpendicular to the length of the foliated unit, see sketched crystals in (B) and (C). The result is that we find a gradual increase in misorientation angle, relative to the first point on the trajectory and a very low degree of misorientation from point to point (B, C). The crystals in (B) and (C) are small, foliated units, while the crystal shown in (D) is a large foliated unit. For the latter crystal (D) we do not find for the crystal portion that is scanned with EBSD such a clear-cut gradual rotation in crystallographic axes orientation, but rather, for adjacent crystallites (possibly folia) an abrupt tilt between two crystallographic axes orientations (see the sketched crystals in (D)). This is also observable from the misorientation angle-distance diagrams (E). Even though an increase in the degree of misorientation angle, relative to the first point on the trajectory, is still present in the misorientation angle - distance diagrams (D), the gradual increase in cumulative misorientation angle, with distance away from the first point on the trajectory, is not as smooth, as it is for the foliated units shown in (B) and (C). In addition, we find, for the crystal in (D) a large degree of misorientation from crystallite to crystallite, from folium to folium. Note as well that the degree of misorientation, relative to the first point as well as from point to point is different for the crystals given in (B), (C), (D) thus, different for the different parts of the foliated shell. The degree of misorientation between adjacent crystallites increases significantly with distance away from the inner shell surface.

Figure 5A gives for the foliated shell layer of *H. hyotis* a large EBSD scan which extends from the inner surface of the shell well into the foliated section of the shell. We find a marked increase in crystal size when moving away and inward from the inner surface of the shell. The consequence of the latter is that, while the smaller foliated units are scanned fully with the chosen size of the EBSD scan, the large foliated crystal units are scanned only in part; the EBSD measurement covers only a portion of the large foliated units. The red, yellow and white stars in the map shown in Fig. 5A point to foliated units that will subsequently be described in more detail. These three foliated units were deliberately taken from different parts of the EBSD map and were selected for their difference in size as well as position in the foliated shell layer. We show, for the selected foliated units, with sketched crystals and pole figures the orientation pattern of calcite c- and a*-axes. For the foliated units given in Fig. 5B, C we see clearly the gradual rotation of calcite c- and a*-axes with the length of the foliated unit and, to a lesser degree, the rotation of crystallographic axes perpendicular to the length of the foliated unit (see the corresponding pole figures and sketched crystals).

Figure 5 gives misorientation angle distributions for individual foliated units along trajectories from a to b and c to d. Trajectories a to b (indicated with white arrows on the foliated units) run parallel to the length of a foliated unit, trajectories c to d (indicated with red arrows on the foliated units) run orthogonal to the length of a foliated unit.

We show two types of misorientation angle distributions with the lengths of the foliated units:

(i) with the misorientation angle relative to the first point on the trajectory the overall, cumulative, misorientation angle is given for a foliated unit, while

(ii) with the misorientation angle from point to point on the trajectory the local, internal, misorientation angle is given for a foliated unit; hence, the misorientation angle from crystallite to crystallite or/and from folium to folium.

(iii) In addition, we give for each misorientation angle diagram the corresponding misorientation angle gradient (the value in the misorientation angle diagram).

We observe the following main features from the misorientation angle diagrams (Figure 5):

(i) Irrespective of the orientation of the trajectory, we find for both cumulative and local misorientation, an increase in misorientation angle with the increasing length of the trajectory.

 doi:10.20944/preprints202502.0108.v1

(ii) The latter is lowest for the foliated unit shown in Fig. 5B (the unit that is closest to the inner surface of the shell), is slightly higher for the foliated unit shown in Fig. 5C and is highest for the foliated unit shown in Fig. 5D (the unit that is most far away from the inner surface of the shell).
(iii) The increase in misorientation angle is smoother when the trajectory runs parallel to the length of the foliated unit, relative to a trajectory that runs orthogonal to the length of the foliated unit.
(iv) When the trajectory is orthogonal to the length of the foliated unit and spans across many folia in the foliated unit, then the increase in cumulative misorientation angle is rather irregular and not smooth.
(v) For all investigated foliated units, we find, irrespective of the direction of the trajectory, similar low misorientation angle gradients.

The crystal shown in Fig. 5D is, in the chosen EBSD scan field (Fig. 5A), most far away from the inner surface of the foliated shell and is, relative to the other crystals (given in Fig. 5B, C), largest in size. It should be kept in mind that we cover only a part of the crystal with the size of the conducted EBSD measurement. For the crystal portion shown in Fig. 5D, we find a different internal structuring, as visualized with the corresponding sketched crystals, pole figures and misorientations. For that crystal portion (Figs. 5D, 6B) we do not see any more a rotation from folium to folium, from calcite c- and a*-axis to calcite c- and a*-axis, as it is the case for the crystals shown in Fig. 5B, C, but mainly the tilting between two crystal orientations (see the sketched crystals, the poles and misorientation diagrams of Fig. 5D). For the crystal portion shown in Fig. 5D we observe two interdigitating substructures, however, these closely related in orientation to each other (see pole figures in Fig. 5D). In the corresponding misorientation diagrams (Fig. 5D) we find, for both trajectories (a to b, c to d), an increase in cumulative misorientation with distance away from the first point on the trajectory, however, the course of the increase in misorientation is strongly jagged (not smooth, as it is the case for the crystals shown in Fig. 5B, C) and we observe formation of a larger degree of misorientation from point to point, between the adjacent crystallites (see misorientation diagrams in Fig. 5D). The following explanation might explain the structural difference for the crystals shown in (C) and (D) on the one hand side, and (E) on the other. The foliated units in Fig. 5B, C are individual blocks/units of co-oriented folia, the crystal portion of the foliated unit in Fig. 5D is a zoom-in into a foliated unit and we observe the interdigitation of two adjacent subunits, calcite c-axes of these subunits being tilted to each other by about 30°.

The texture of the foliated crystal units, irrespective if these are small or large, is very specific (see pole figures in Figs. 6, 7, S4). We observe for an EBSD scan, comprising various foliated crystal units a ring in c-axis as well as a ring in a*-axes orientation (black arrows in pole figures shown in Fig. 6C, D). With Fig. 6 we attempt to visualize how the ring in c- and a*-axes orientation is generated for an assembly of adjacent foliated units. When reduced to the core crystal of a large foliated unit (Fig. 6B), we see in the pole figure a cluster in c-axis and three clusters in a*-axes orientation. Nonetheless, for the clusters in the pole figure and in the corresponding EBSD map we observe that the core crystal of the foliated unit consists of two, differently oriented, subunits. When two to three adjacent foliated units are regarded, we find that each of these is structured by interdigitating subunits and that, in turn, each foliated unit adds in the pole figure a cluster in c- and three clusters in a*-orientation. Hence, for a 3D assembly of adjacent foliated units the c- and a*-axes clusters of the different foliated units merge and generate a ring-shaped c- and a*-axes orientation distribution. Although not as well observed as for the large foliated units, the small foliated units are also interdigitations of adjacent, substructured foliated units and for these we see as well the generation of c-axes and a*-axes rings in the pole figure (see pole figures in Fig. 7B, C, D). Nonetheless, as the EBSD scan covers many, to each other strongly misoriented, small foliated units, the ring-shaped c- and a*-axes orientation distribution for small foliated units is rather noisy, not as clear-cut as it is the case for the large foliated units (compare the pole figure shown in Fig. 7B with that shown in Fig. 7C).

 doi:10.20944/preprints202502.0108.v1

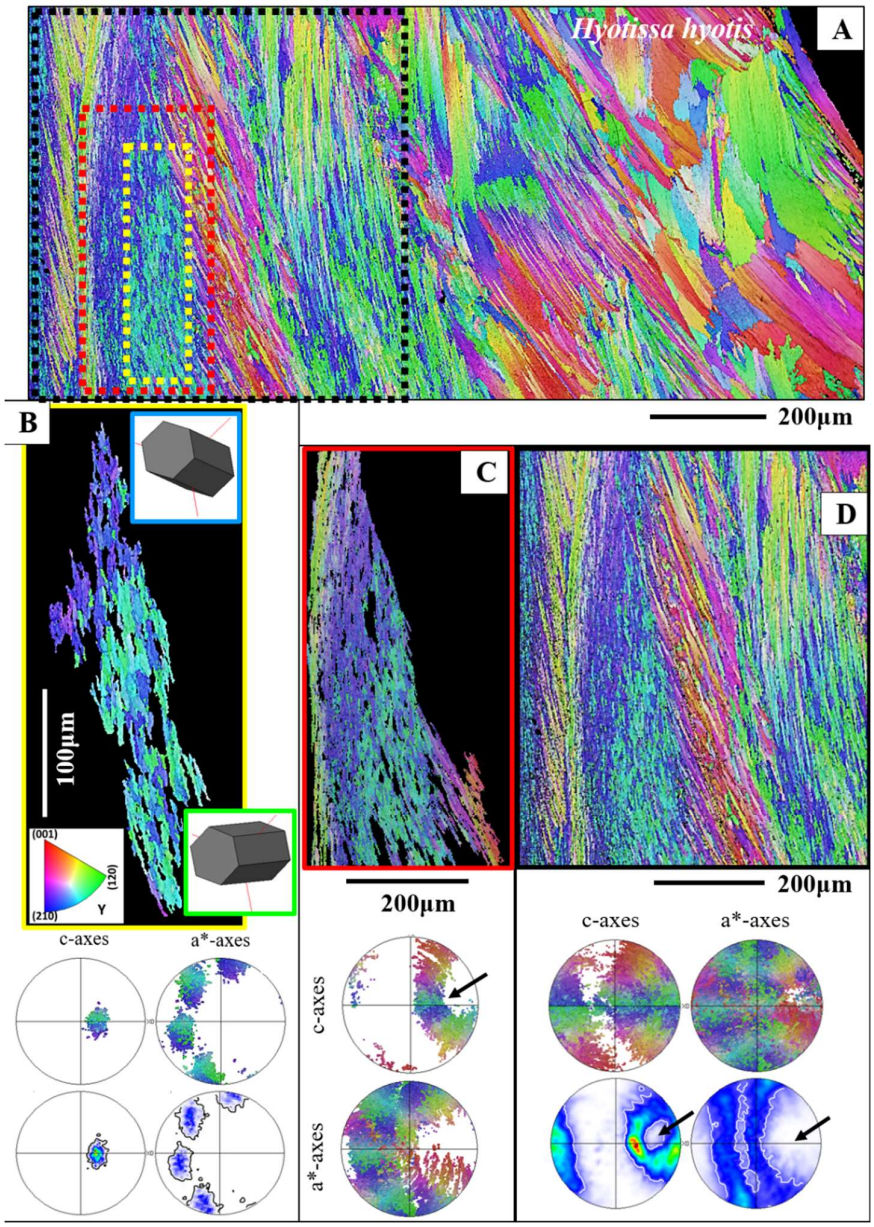

Figure 6. The microstructure of large foliated units (B to D) and the nature of their texture (B to D). Formation and development of c- and a*-axes orientation rings for the texture pattern of the foliated units (B to D). The colors in Figure 6 code for crystal orientation. The core crystal entity (e.g. as that shown in (B)) of a large foliated unit is a structured arrangement of crystallites and consists of an interwoven meshwork of, mainly, two subunits having slightly different orientations (see blue and green colors in the map and pole figure in (B), see the sketched crystals in (B). Nonetheless, we find in the corresponding pole figure (B) a cluster for c-axes and three clusters for the a*-axes orientations. However, we observe well in the pole figures (B) that the c- and a*-axes clusters are substructured. Selecting a larger section of a foliated unit (C), e.g. the core crystal entity and adjacent foliated crystals (C), in the pole figures we find that additional c- and a*-axes clusters are added to the c- and a*-axes clusters of the core crystal entity, in such a way that the c- and a*-axes orientations of a few adjacent large foliated units form a ring in the c- and a*-axes pole figures (black arrows in C, D). This is a very specific texture pattern and very different to the texture of fibrous, columnar and nacreous biocalcified microstructures, where the texture pattern of the latter microstructures is axial. A: The entire EBSD scan, with the colors indicating crystal orientation. The dashed yellow, red and black rectangles in (A) depict the EBSD scan portions that are shown in (B), (C) and (D).

 doi:10.20944/preprints202502.0108.v1

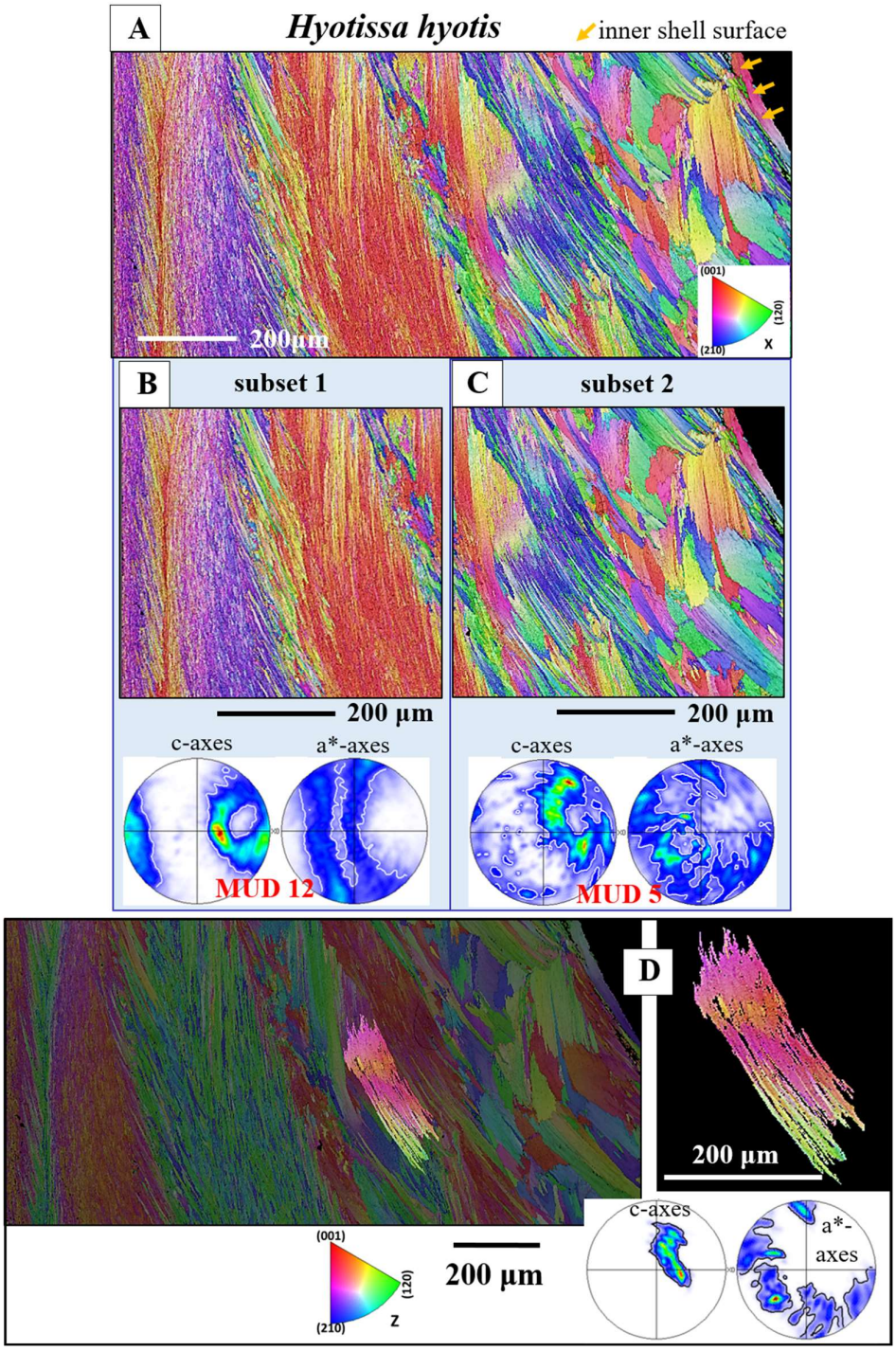

Figure 7. The texture pattern of assemblies of large and small foliated units (A to C) and the texture of an individual small foliated units (D). We observe for all foliated units, small or large, the same texture pattern, namely, formation of c- and a*-axes orientation rings in the corresponding pole figures. The outline of the c- and a*-axes orientation rings is very irregular for small foliated units (C), due to their high abundance and almost random orientation organization (MUD of 5 (C)). We find also formation of c- and a*-axes rings for an individual small foliated unit.

 doi:10.20944/preprints202502.0108.v1

As demonstrated in Fig. 4E, F, we find for the foliated units a gradation in calcite c- and a*-axes. This points to a mesocrystalline nature of the foliated units. A mesocrystal is defined as a mesoscopically structured crystal consisting of submicrometer-sized crystallites, with a crystallographic register [35,36,40]. The distinction of the individual nanocrystals is not clearcut because the crystal lattice is continuous across them [40]. The length, width, and thickness of crystallites that form a mesocrystal do not have to be similar in size [40], as it is the case for biologically-formed mesocrystals, e.g., the foliated units of Ostreoidea shells. For the generation of a mesocrystal, the change in crystallographic axes orientation needs to have a, in 3D, controlled tilt [40], and this we find for the foliated units of the investigated Ostreoidea shells. For individual foliated units, we see in the relative frequency - misorientation angle diagrams only low-angle (up to 10°) misorientations and a very small range in misorientation angle (Fig. 4E, F).

Figure 8 shows an EBSD scan that covers many foliated crystals and extends from the inner shell surface well into the foliated shell layer. We see in this measurement how inner shell surface curvature is generated with foliated units. It is formed with a decrease in foliated unit size towards the curved surface thus, at the curved surface, we find an accumulation of small foliated units.

 doi:10.20944/preprints202502.0108.v1

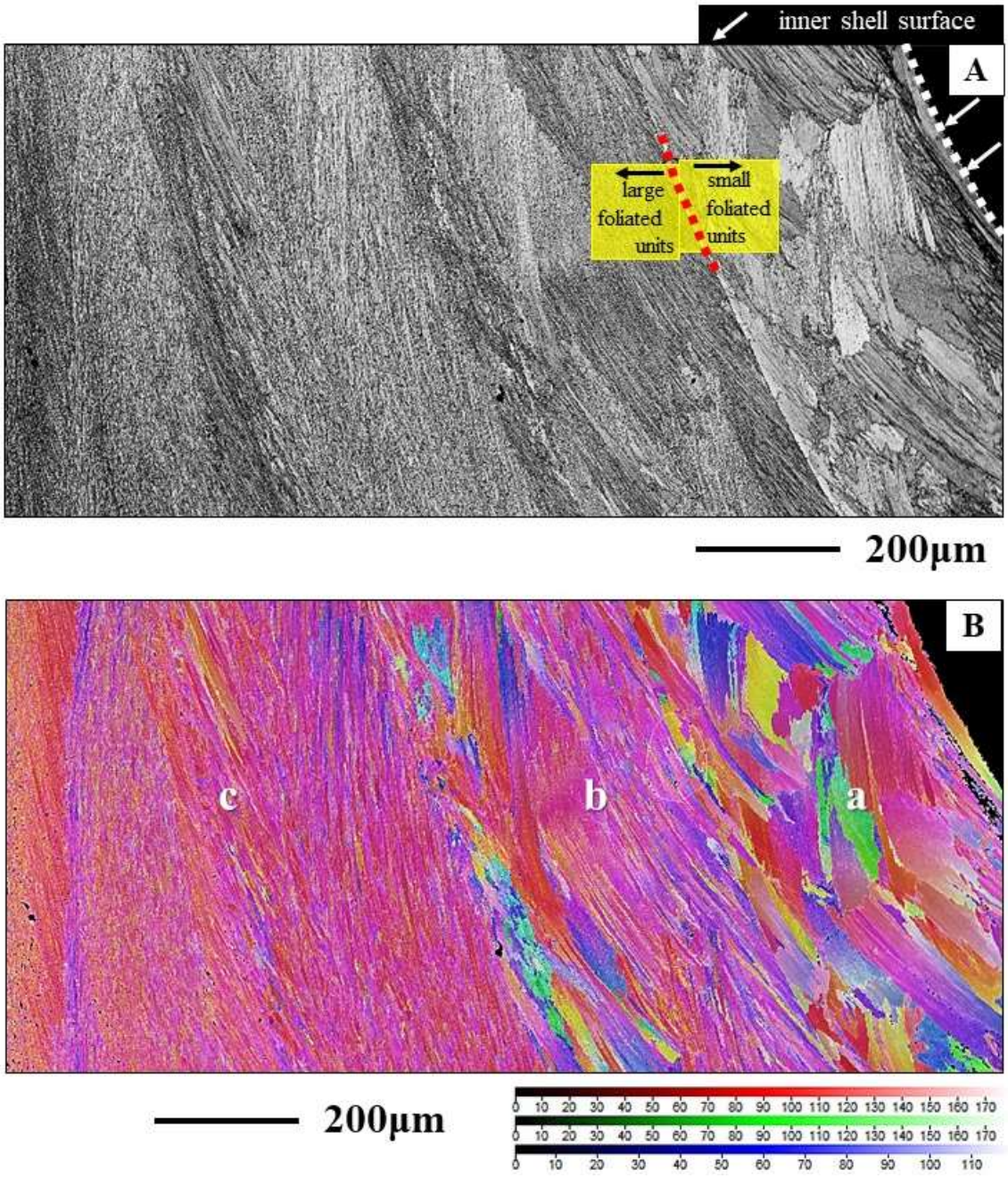

Figure 8. The *Hyotissa hyotis* distribution pattern of small and large foliated units (A, B) and generation of a curved inner shell surface with foliated units (A, B). A: EBSD band contrast measurement image; B: for calcite orientation color-coded EBSD scan. For the scan shown in (B), we use the Euler angle coloring code. It is well observable that towards the inner shell surface the size of foliated units decreases gradually, hence, a curved surface is formed with an assembly of small foliated units, in contrast to the size of foliated units that are present in more outward sections of the foliated shell layer. We appear to find layers formed of small (a), larger (b) and very large (c) foliated units (B).

 doi:10.20944/preprints202502.0108.v1

Figure 9 gives calcium carbonate phase, microstructure, texture and crystal co-orientation strength of granular to prismatic crystals that comprise the shell at the attachment sites, myostraca, of pallial and adductor muscles. We observe for these aragonitic shell sections a different Ca-carbonate phase, as that of the calcitic rest of the shell (Fig. 9A, F), a specific microstructure (Fig. 9C, E), which is distinct from that of the rest of the shell, an axial texture (see pole figures for aragonite in Fig. 9C, E), a higher crystal co-orientation strength, as observed for all other shell portions (see MUD values in Fig. 9C, E) and a marked peak at 64° misorientation in the misorientation angle diagram (black arrows in Fig. 9C, G). The crystallographic-structural difference between myostraca and the other valve sections is the result of different calcium carbonate hard tissue forming determinants (e.g., [37,38]).

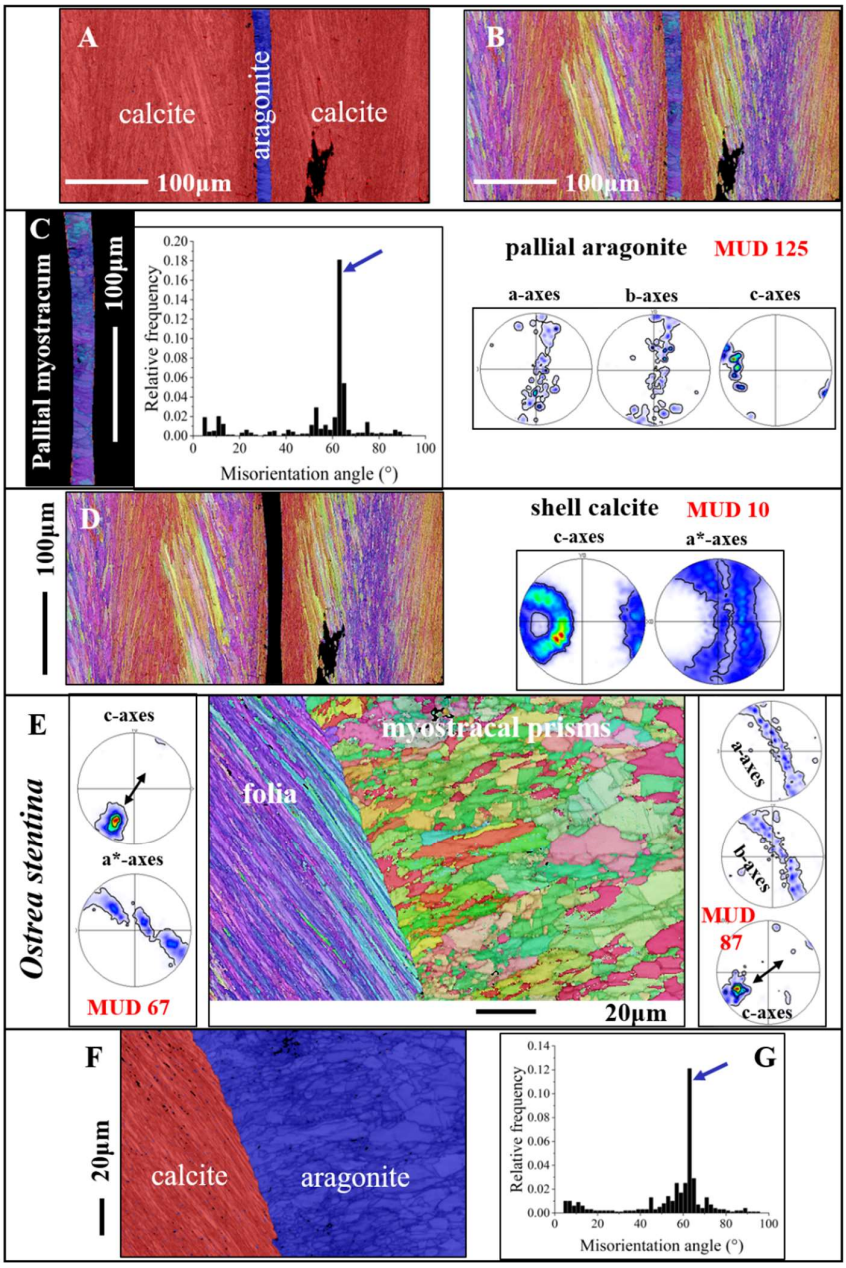

Figure 9. The microstructure, texture, and carbonate phase of ostreoidean adductor and pallial myostraca (A to G). A, B: *Ostrea stentina*. The myostraca are formed of aragonite prisms (A, F). These have a characteristic

 doi:10.20944/preprints202502.0108.v1

microstructure derived from their growth process [39, 40], form an axial texture (see pole figures for aragonite in C and E), and are characterized by a marked peak at about 63° to 64° misorientation in the relative frequency-misorientation angle diagram (black arrow in C, G). The latter indicates the twinning of the aragonite on the {110} plane. In comparison to shell calcite, myostracal aragonite crystals are more co-oriented (see the difference in MUD value between myostracal aragonite (C, E) and shell calcite (D). Black arrows in the pole figures shown in (E) indicate the direction of c-axis orientation for foliated calcite and myostracal aragonite. We find for the two microstructures some correspondence in c-axes orientation.

Figures 10 to 13 and Fig. S6 visualize the structural arrangement of calcite crystals when voids, and pores are incorporated into Ostreoidea shells. Ostreidae incorporate a meshwork of calcite in between stacks of folia, Gryphaeidae occlude lenses of vesicular pores within the stacks of folia. When based on SEM images, the crystal meshwork of the chalk appears to be entirely unstructured (Fig. 10A to C). This is the case to a large degree, as indicated by the large-angle misorientations in the relative frequency-misorientation angle diagrams (Fig. 10E, F). However, we also observe some structuring of the chalk by larger-sized blades/struts (see EBSD measurements in Fig. 11D). We often find low MUD values for the chalk (e.g. MUD 4; Fig. 10F), but also an increased MUD (e.g. MUD 45, Fig. 11D; MUD 24, Fig. 11E). Thus, the crystallites that comprise the chalk are not at all entirely random in orientation. High-resolution EBSD measurements demonstrate the presence, when based on structure, of a transitional zone between the foliated crystals and the calcite meshwork of chalk (white stars in Fig. 10D, Fig. 10G, Fig. 11B). The structure of this transitional zone is chaotic, we do not find in the latter the typical structure of either foliated crystals, or of the calcite meshwork of the chalk (e.g., 11A to C). Regarding crystal organization for the topologically closely-related foliated, transitional and chalk crystal arrangements (Fig. 11A to C), we observe a rotation in c-axis orientation from the folia (Fig. 11C) to the crystals at the transition from the folia to the chalk blades/laths (Fig. 11B). While c-axis orientation of calcite folia is rather within the plane of view (green to yellow data points in the pole figure in Fig. 11C), it becomes gradually tilted out of the plane of view and being oriented perpendicular to the plane of view when approaching the transitional section to the chalk (yellow to red data points in the pole figure in Fig. 11C). Calcite c-axis orientation of the transitional zone between the folia and chalk is mainly perpendicular to the plane of view (red data points in the pole figure in Fig. 11B).

 doi:10.20944/preprints202502.0108.v1

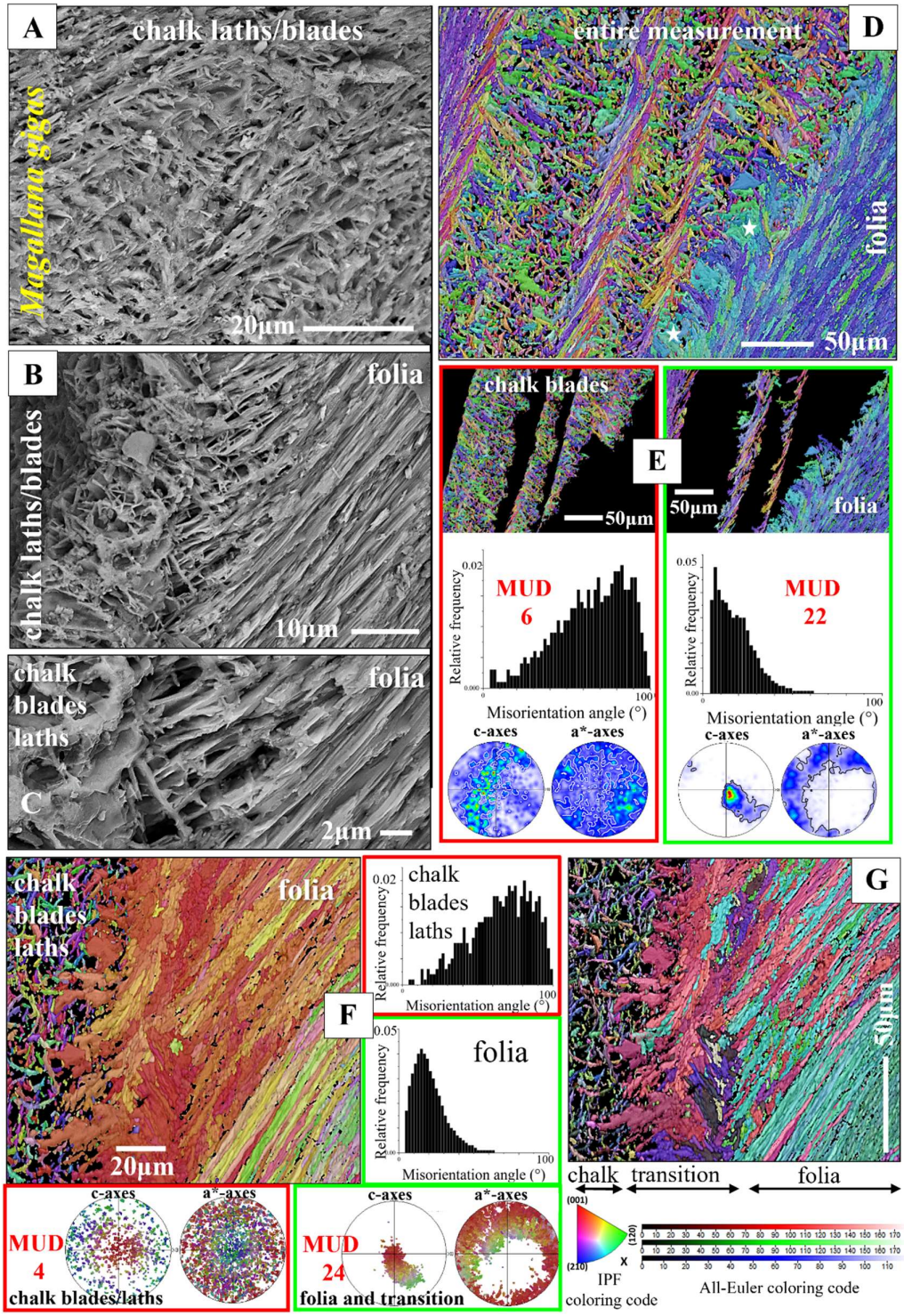

Figure 10. The meshwork of crystals, and their microstructure and texture, that form chalk lenses in Ostreidae shells (A to C) and the crossover from the foliated to the chalk-related assembly of calcite (B to G). A to F: *Magallana gigas*. A to C: BSE micrographs; D to G: EBSD maps, color-coded for crystal orientation; corresponding pole figures, showing orientation data (F) or their density distribution (E). For the microstructures and textures, we show the corresponding relative frequency-misorientation angle diagrams. Crystal co-orientation strength is given with MUD values (D, E). For the EBSD map shown in (F), the IPF coloring code was used, for the map given in (G), the all-Euler coloring code was selected. Although both microstructures are formed of blade/lath-shaped crystals, we find significant differences in crystal texture, magnitude of misorientation angle, and mode

 doi:10.20944/preprints202502.0108.v1

of misorientation angle distribution (D, E). Even though the assembly of folia is more co-oriented than the assembly of crystals that form the chalk, crystal co-orientation strength is low for both microstructures (see MUD values). We find between the stacks of folia and the agglomeration of chalk blades/laths a transitional zone (G, white stars in D and Fig. 11B), marked by a chaotic microstructure, not resembling in structure either the arrays of folia, or the aggregation of chalk blades/laths. At EBSD data acquisition and EBSD data evaluation the three Euler angles were kept at 0°; ϕ1=0°, Φ=0°, ϕ2=0°.

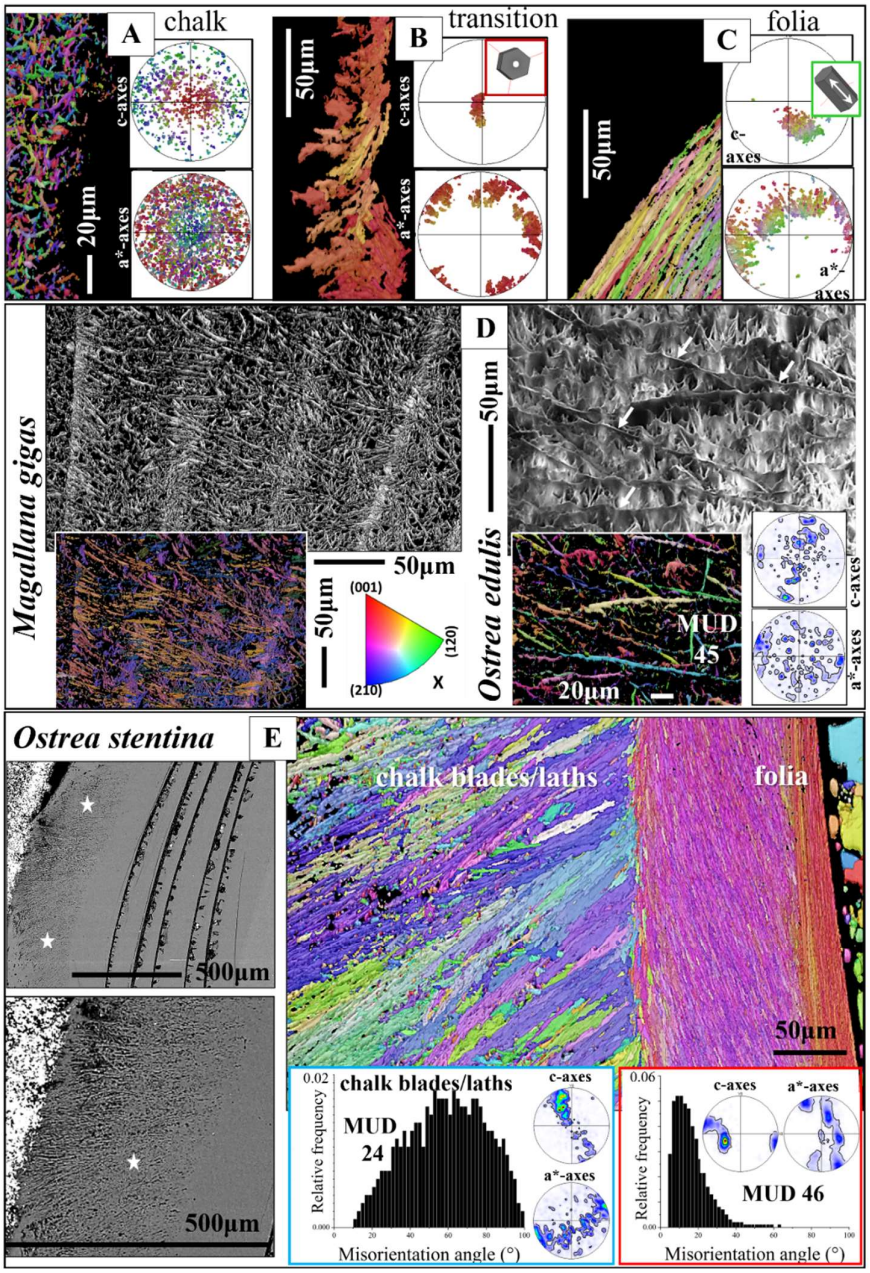

Figure 11. A to C: Subsets of the EBSD measurement shown in Fig. 10F highlight the difference in crystal orientation between the blades, laths of the chalk (A), the crystals that form the transitional section between the chalk and the stacks of folia (B) and for the stacks of folia (C). In the shell, these microstructures are adjacent to each other. Sketched crystals visualize calcite crystallographic axes orientation of the folia (C) and of the crystals that form the transitional section between the folia and the chalk blades (B). Calcite c-axes of the latter are perpendicular to the plane of view (B), while calcite c-axes of the folia are largely within the plane of view (C). D, E: Meshwork of chalk blades and laths within the foliated shell layer (D) as well as adjacent to the foliated

 doi:10.20944/preprints202502.0108.v1

layers at outer shell sections (E). The co-orientation strength of calcite crystallites that comprise the chalk is low but not random (see MUD values for the chalk in D, E). Thus, there is some structuring of the chalk, e.g. by struts (see EBSD band contrast and crystal orientation maps in D). E: A chalk-type microstructure at outer shell layers (white stars in E), developed with an axial texture (pole figure for the chalk in E), a slightly increased crystal co-orientation strength (MUD value for the chalk in E) and the typical relative frequency-misorientation angle pattern that is also observed for the chalk within the lenses that are incorporated into the foliated shell. This is the first report of a chalk-type microstructure at outer shell layers. A to C, inserts in D, E give EBSD maps, coded for crystal orientation. The micrographs in (E) and the left-hand side, grey-scaled, image in (D) are BSE images. The right-hand side, grey-scaled, image in (D) is an EBSD band contrast measurement image. At EBSD data acquisition and EBSD data evaluation, the three Euler angles were kept at 0°; $\phi1$=0°, Φ=0°, $\phi2$=0°.

Our study shows that calcite with a chalk-like microstructure is not only present in lenses within the foliated shell. We observe for *O. stentina*, formation of a layer with a chalk-like microstructure, texture, and misorientation angle distribution also at outer shell portions (Fig. 11E), however, always in topological relation to the foliated shell layer (EBSD map in Fig. 11E). Figs. 12, 13 show for *H. mcgintyi*, *H. hyotis*, and *N. cochlear* the mode of crystal organization around voids and pores (e.g., Fig. 12B, 13B, C). The calcite microstructure that surrounds the pores consists of an assembly of dendritic crystals (Figs. 12, 13). These are very diverse in size (e.g., Fig. 13B) and, in particular, have highly fractal morphologies (e.g., Figs. 12B, D, 13B). Adjacent crystals interlock strongly in 3D with neighboring fractal crystals (Fig. 12D, 13B). The calcite of individual dendritic crystals is well co-oriented (Fig. 13C), hence, we find for individual dendritic crystals only low-angle misorientation (Fig. 10E). Even though crystal co-orientation strength within an individual crystal is high, due to the, more or less, random interconnection of crystals, crystal co-orientation strength of the whole microstructure is low (Figs. 12A), nonetheless, it is comparable to that of the adjacent foliated shell (Figs. 13A). The texture of the dendritic granular microstructure has a very low preferred orientation, thus, a very weak texture (pole figures in Fig. 13A, C). Nonetheless, in rare cases we see for the assembly of dendritic crystals the development of a weak axial texture (pole figure in Fig. 12A). Thus, for the latter example, we see a directed assembly of dendritic crystals, however, irrespective of which texture is developed, with a very decreased crystal co-orientation strength (see the low MUD values for the measurements in Figs. 12A, 13A, C).

 doi:10.20944/preprints202502.0108.v1

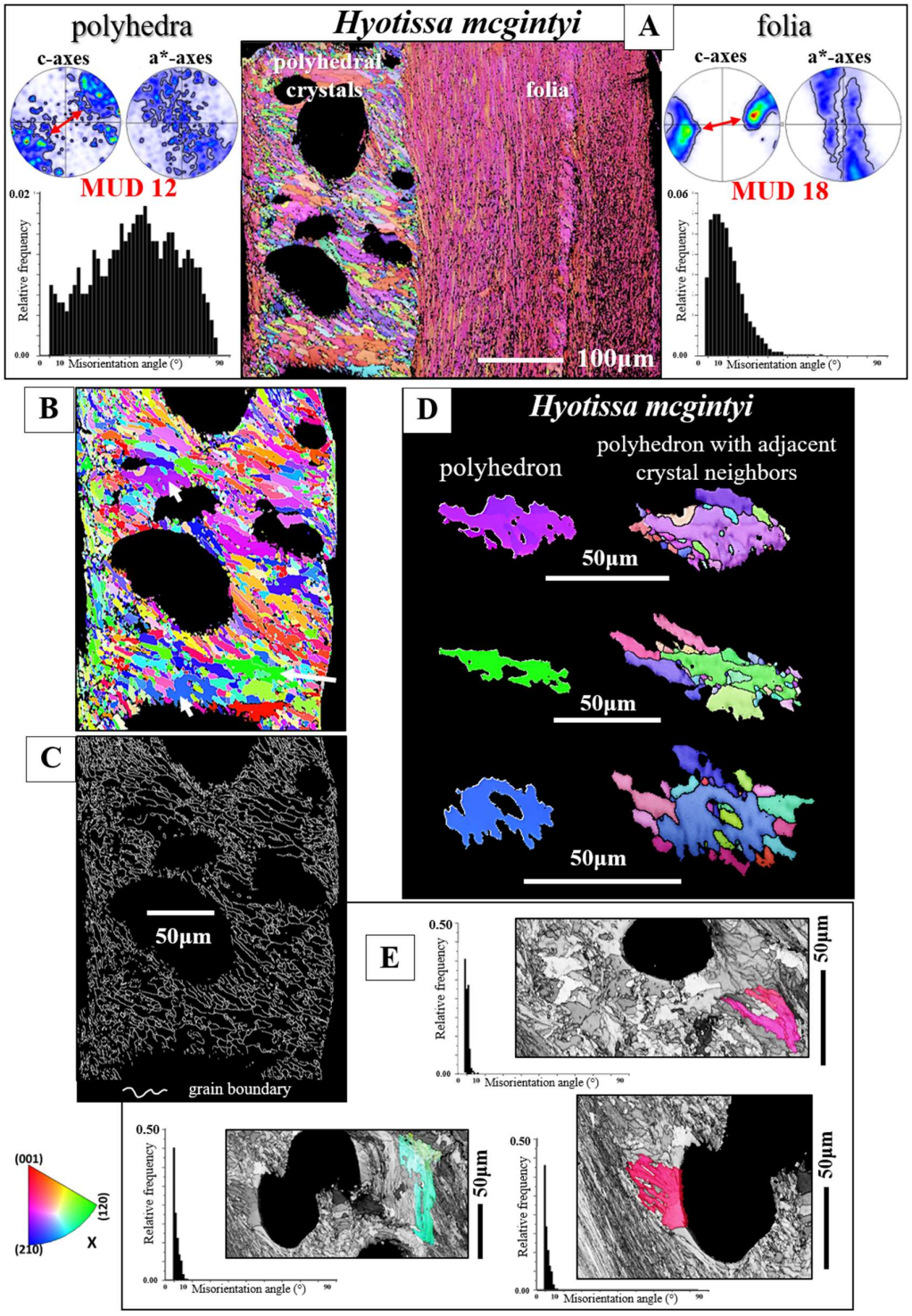

Figure 12. The crystals, their size, morphology, microstructure and texture that encase the vesicular pores, incorporated into the shell of the gryphaeid species *Hyotissa mcgintyi* (A, B, E). Although crystal co-orientation strength is very comparable between the foliated and the dendritic, polyhedral crystal, shell portion (A), we find, for the two shell layers, significant differences in microstructure, texture and misorientation angle distribution (A). The transition from folia to dendritic crystals is abrupt (A). Note the axial texture for the dendritic, polyhedral crystal, shell portion. Dendritic crystals have highly irregular, fractal morphologies (B, D). Adjacent

 doi:10.20944/preprints202502.0108.v1

dendritic crystals interdigitate strongly (D). The three white arrows in the EBSD map in (B) point to the crystals shown in (D). (C): The white lines are the traces of dendritic grain boundaries for the grains shown in (B) and highlight the tight interlinkage of neighboring grains as well. E: Relative frequency-misorientation angle diagrams for selected dendritic crystals. Note the low degree of misorientation angle between calcite crystallites in a dendritic crystal and the similarity of misorientation angle distribution pattern to the misorientation angle distribution pattern of a foliated crystal (compare to Fig. 4E, F). Red arrows in the pole figures in (A) indicate the overall direction of c-axis orientation. Even though being at an angle of a few degrees, there is some correspondence in c-axis orientation between the foliated shell and the adjacent dendritic crystal shell layer. At EBSD data acquisition and EBSD data evaluation, the three Euler angles were kept at 0°; $\phi1=0°$, $\Phi=0°$, $\phi2=0°$.

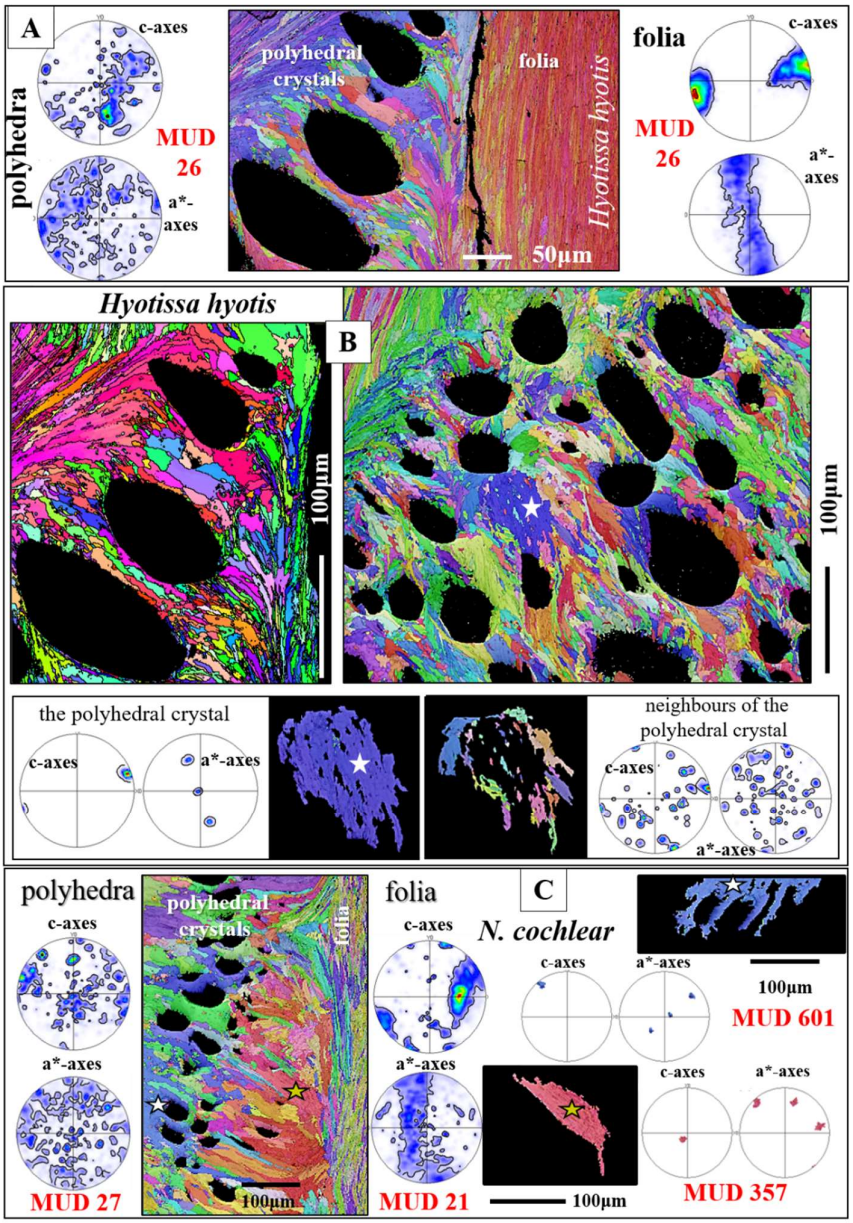

Figure 13. Assembly of fractal-shaped (dendritic) crystals that surround the vesicular pores in *Hyotissa hyotis* and *Neopycnodonte cochlear* (Gryphaeidae) shells (A to C). Dendritic grains vary strongly in size, shape and orientation. The dendritic, polyhedral, crystal texture pattern is distinct from that of the foliated shell (see pole figures in A). B: Strong interlinkage of dendritic crystals, well visible from the EBSD maps as well as from individual crystals. For the latter see the crystal marked with a white star in (B) and its adjacent neighbors. C:

 doi:10.20944/preprints202502.0108.v1

The calcite of individual grains (indicated with a yellow and a white star in C) is well co-oriented. EBSD map in (C): The assembly of folia lashes out into the adjacent dendritic granular layer, encasing the vesicular pores. At EBSD data acquisition and EBSD data evaluation the three Euler angles were kept at 0°; ϕ1=0°, Φ=0°, ϕ2=0°.

Calcite crystals within the cementation layer are mainly granular (Fig. 14A); when slightly larger-sized (Fig. 14B), the morphology of the cementation layer crystals tends to be prismatic (Fig. 14B). Crystal co-orientation strength for the cementation layer crystals is low (see MUD values in Fig. 14A, B). Crystal texture can be very vaguely axial (pole figure in Fig. 14B). However, the axial texture can also be developed with some directed c- and a*-axes orientation (pole figure for the granules in Fig. 14A).

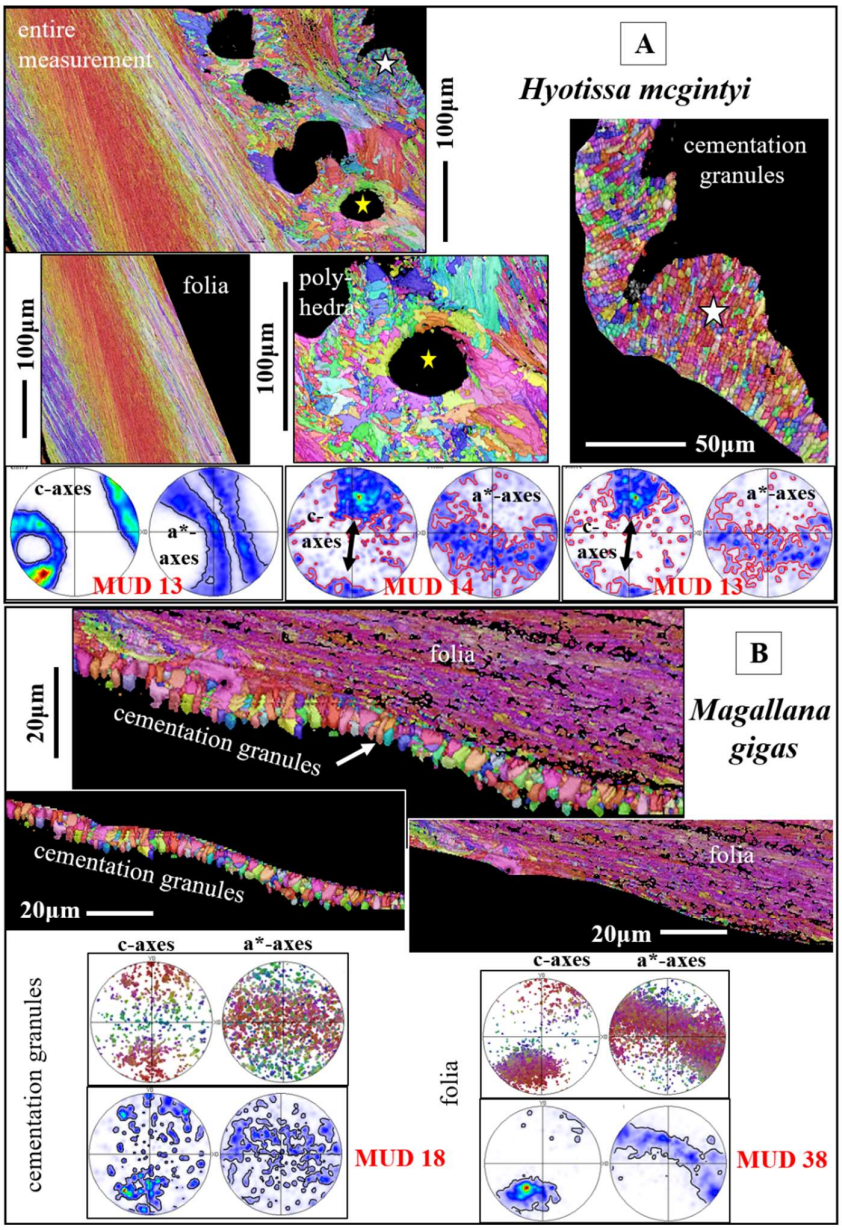

Figure 14. A, B: Morphology, microstructure, texture and co-orientation strength of crystals that reinforce the biopolymer glue of *Hyotissa mcgintyi* (Gryphaeidae) and *Magallana gigas* (Ostreidae) which cements the shell to

 doi:10.20944/preprints202502.0108.v1

the substrate. White star in (A): The granular nature of the cementation layer and the arrangement/assembly of granules into chains/strings. We observe from the pole figures some oriented arrangement of the cementation granules as well as for the adjacent assembly of dendritic crystals (A). Black arrows in the pole figures in (A) indicate the overall direction of c-axis orientation of the granular (the cementation granules) and of the dendritic granular calcite (the calcite encasing the pores). At EBSD data acquisition and EBSD data evaluation, the three Euler angles were kept at 0°; ϕ1=0°, Φ=0°, ϕ2=0°.

Crystal organization of the rhombohedra (Fig. 1G) is not discussed in this contribution, but in detail in Sancho Vaquer et al. 2025 [13].

3. Discussion

At fabrication of structural materials it is a challenge to obtain the right balance between strength, toughness and resilience (e.g., [43]). Nonetheless, is a balance attained, it is often determined, to a large extent, by the design of the structural material in question (e.g., [44–48]).

The strength and toughness of a structural material can be changed in many ways, e. g., (1) by incorporating impurities into the crystals, (2) by varying crystal size and crystal organization, (3) by forming composites out of different minerals, (4) by generating composites of organic substance and mineral, or (5) by incorporating interfaces into crystals or into crystal microstructures [45,47,48].

Driven by evolution-, environment- and predation, a large variety of biologically secreted materials evolved in the geological past. These are characterized by an advanced material performance which is called forth by (1) their, in three-dimension, hierarchical architecture, (2) by bridging a wide range of scale levels and connecting the atomic scale to the macro scale (e.g., [45,48] and (3) by fabricating composites, in particular, of biopolymers and minerals. Apart from myostracal and ligament aragonite, that are by volume very minor shell components of Ostreoidea shells, all the Ostreoidea form their shell of low-Mg calcite [16–18]. Hence, Ostreoidea do not vary the carbonate phase of their shell material for the attainment of a balance between strength, toughness and resilience, but, mainly, the design and the architecture of the different shell layers, that is, the morphology, size, interlinkage of crystals (microstructure) and the mode of crystal assembly in the different layers and portions of the shell (texture) (Figs. 1-14, S1-S6).

3.1. The microstructures

The Ostreoidea secrete for shell generation crystals with many shapes: columns, prisms, granules, rhombohedra, dendrites, laths with arrowhead endings, folia, foliated units, blades, and form out of these six different microstructures and five different textures (Figs. 1 to 14). Apart from the myostracal aragonitic microstructure, all calcitic microstructures have a low crystal co-orientation strengths, varying, for the measurements conducted in this study, from an MUD value of 4 to an MUD of 67 (Table 1, Figs 1 to 14). Nonetheless, when individual crystals or crystal units are regarded, e.g. rhombohedra, dendrites, folia, individual foliated units, individual columns, the crystal co-orientation strength of these is very high (e.g. Figs. 3J, 13C, Table 1). Thus, little co-oriented is the assembly of the crystal units that form a shell layer, while the calcite of individual units is highly co-oriented. The low crystal co-orientation strength of the different shell layer microstructures is striking, in particular, when compared to the co-orientation strength of other bivalve shell microstructures, where MUD values (for a particular microstructure) scatter between 200 and 400 [45,48]. The low crystal co-orientation strength of Ostreoidea shell microstructures is not just the result of fast shell secretion, thus, the necessity to form a thick shell in short time. The low MUD values of some Ostreoidea microstructures can be explained with the specific use and utilization of a particular shell layer, as it is the case for the assembly of columns, for the assembly of granules and for the assembly of the dendritic crystals.

 doi:10.20944/preprints202502.0108.v1

Table 1. The different crystals that comprise Ostreoidea shells and the range of crystal co-orientation strength, expressed as MUD value, for individual crystals as well as for a particular microstructure. When the MUD value of a microstructure is considered, then we observe the highest crystal co-orientation strength for the myostraca and the lowest for the chalk and for the polyhedral crystals. When the MUD value of individual crystals is considered, we find the highest crystal co-orientation strength for individual rhombohedral crystals, followed by the individual prisms of the myostraca.

	MUD value of an EBSD scan covering many crystals	MUD value of an EBSD scan over an individual crystal
Columnar crystals	25-30	250-460
Foliated crystals/crystallites	18-67	Folium: 591, 626 Foliated crystal: 174, 545
Pallial prisms	125-130	650-680
Adductor prisms	85-90	650-700
Chalk blades/laths	4-45	450-500
Polyhedral crystals	12-27	350-600
Cementation granules	13-18	600-650
Rhombohedral crystals	-	700, >700

3.1.1. The microstructures that form the compact shell layers

The columnar shell layer

The columnar layer consists of closely packed, discrete, column-shaped large calcite units, in some references termed also as prisms. In cross-section, individual columns have polygonal morphologies (Fig. 3D). The columns are variable in size (Fig. S1A, B). In general, their arrangement in the layer is such that, towards outer columnar layer surface, the columns decrease in size. For the investigated species, we found that the outermost shell layer surface is seamed by rather small-sized columns, which increase in size toward the boundary with the foliated shell layer (Fig. S1A, B).

We find two main structural characteristics for the columnar layer of the investigated Ostreoidea species.

1. The columnar layer is strongly enriched in organic substance. The latter is developed as thick membranes delineating adjacent columns (Figs. 35, 37 in [17], and [48]). In addition, we observed that much organic substance is also present within the columns, e.g. Fig. 3B, C. Surprisingly, the deposition of organic substance in the columns has a banded appearance (Fig. 3A to C) and is not inhomogeneous as it is the case for bivalve aragonitic columnar prisms (e.g. *Elliptio crassidens* (Lamarck, 1819) [32]). The growth bands in Ostreoidea columnar layers are episodic growth bands. Harper and Checa [48] investigated the organic content of the shell layers of pearl oysters (very many species of 29 taxa). These form their shell of columnar calcite and nacreous aragonite. The authors detected a significant difference in organic substance content between the columnar and the nacreous shell layers and suggested that the high percentage of organic substance of the columnar layer, relative to the nacreous shell layer, might be regarded as a functional trait. The more organic substance-rich and, thus, more ductile, columnar layer renders the structural flexibility of that shell layer and is of use for, e.g., a tight closure of the valves. Thus, a more efficient protection of the soft tissue and organs from organism-related and/or physical, external, attack.
2. The other structural characteristic that we observed for the columnar layer of the investigated species is the strong structuring of the columns (Figs. 3E, F, S3). An individual column consists of many subunits, domains. These have very irregular shapes and sizes (Figs. 3E, S3A) and are misoriented to each other by about 5° to 10° (Fig. 3K). The subunits, domains of the columns are formed of platy calcite crystals (Fig. S2). These have strongly irregular morphologies and vary also highly in size (Figs. 3F, S3B, C). It should be noted that, for the species investigated in this study, neither the structuring of the columns into subunits/domains, nor the crystals that

 doi:10.20944/preprints202502.0108.v1

comprise the domains resemble the structures that we find for the corresponding foliated shells. We find very different microstructures and crystal textures for the columnar and for the foliated shell layers. Even though, two structural characteristics are similar for the two shell layers: (i) their very hierarchical architecture and (ii) The high co-orientation strength of calcite crystals in the subunits (Figs. 3J, 4E, F), but very low co-orientation strength of the units (columns, foliated units) in the relevant shell layer (Figs. 3H, I, 7B, C).

The foliated shell layer

For all investigated species, the foliated shell layer comprises the largest part, by volume, of the valves and is outstanding in microstructure and crystal texture (e.g., the results of this study and [16,17,21,28,49,50]). For the foliated shell microstructure, these studies visualized that the crystals of the foliated material are arrowhead terminated laths. These assemble, more or less, in parallel and form foils, consisting of a few laths. Two to three foils form a folium, assemblies of folia form foliated units and a conglomeration of foliated units forms the foliated shell (e.g. Figs. 6, 7). We observe for the foliated shell of the investigated species, for individual foliated units, a gradation in c- and a*-axes orientation (see pole figures in Fig. 4E, F) and, according to the latter, for an assembly of foliated units, a ring-shaped orientation distribution of calcite c- and a*-axes in the pole figures (see the pole figures in Figs. 6 and 7). The latter is, from a crystallographic point of view, a very remarkable structural characteristic. Other organisms, gastropods, bryozoans, also have foliated layers, but their textures are different to the foliated calcite of the Ostreoidea.

The combined interpretation of crystallographic characteristics gained from the Ostreoidea foliated microstructures and the corresponding textures infers the conclusion that the texture pattern of the foliated shell layer of the investigated species resembles a turbostratic arrangement of the folia and of the foliated units. For the description of a turbostratic arrangement of particles see [51,52]. Cumulative misorientation angle patterns along trajectories parallel or/and orthogonal to the length of a foliated unit show that the course of the misorientation angle in the cumulative misorientation diagram is very smooth *with the length* of the foliated unit, while it is ragged when the trajectory runs *orthogonal to the length* of the foliated unit (Fig. 5B, C). The above described structural-crystallographic features indicate that the texture of the Ostreoidea foliated microstructure is not axial or sheeted, nether spherulitic, nor single crystalline. It is rather turbostratic [50], nonetheless, and due to the lath morphology of the foliated crystals, the Ostreoidea foliated texture has, most probably, a specific form of the turbostratic texture motif [53]. The turbostratic textures described for, e.g. aggregates of clay particles and particle units, are based on the notion that a clay particle is a platelet. Many platelets form a clay platelet unit and many of the latter units generate in clay-water suspensions a clay platelet unit layer with a turbostratic texture (very well addressed by Aylmore and Quirk [51] and Lutterotti [52]). The crystals that form the Ostreoidea foliated shell are lath-shaped (Fig. 4B) and only aggregations of these (foils, folia) generate plate-shaped units.

The cementation layer

The cementation layer of Ostreoidea shells has as well a rather compact microstructure, relative to the cavity-rich microstructures of both the chalk and the vesicular lenses. The crystals in the cementation layer of the investigated species are mainly granular and can be regarded to be reinforcements of the organic glue that cements the shell to the substrate, in general, to a rough-surfaced substrate. Although the orientation pattern of the cementation granules is rather isotropic (see the pole figures in Fig. 14B for the cementation granules), in some instances we observed some directed orientation of the granules (see the pole figure for the granules in Fig. 14A) and, as it is shown in Fig. 14A, some co-orientation of calcite c-axes of the cementation granules and the c-axes of the dendritic crystals that generate the shell layer that incorporates the vesicular pores (see the pole figures for the dendritic crystals and cementation granules in Fig. 14A). Our study did not disclose the reason for the low co-orientation strength of the cementation granules. Nonetheless, the low

 doi:10.20944/preprints202502.0108.v1

degree of their co-alignment in the layer is in concert with the low co-alignment of the units (the columnar and foliated units) that form the other Ostreoidea shell layers. Even though, we might hypothesize that the isotropic orientation pattern of the cementation granules is of benefit for cementation of the shell to an irregularly surfaced substrate. From our EBSD measurements we did not observe the ridge-and-furrow structure of the cementation granules, as reported by Yamaguchi [54]. Nor can we confirm the conclusion of MacDonald et al. [27] stating that the cementation granules are precipitated from seawater and are not secreted by the organism. MacDonald et al. [27] justify the latter conclusion with the observations that (i) the cementation granules consist of high-Mg calcite and (ii) that the cementation granules are fully random in orientation. We investigated in great detail the cementation layer of *H. mcgintyi* and *M. gigas* and did not find any difference in Mg-content between the granules and the adjacent folia. In contrast, when EBSD measurements are conducted with high resolution, we observed (i) a tight structural connection between the foliated shell and the adjacent assembly of cementation granules (Fig. 14A, B) and (ii) even some continuity in orientation of calcite c- and a*-axes between the dendritic and the cementation granular shell layers (Fig. 14A). As shown in this as well as in other studies [32], not all Ca-carbonate skeletons/skeletal elements have or need to have a high crystal co-orientation strength. It is not uncommon and also not of disadvantage for the organism to secrete a carbonate hard tissue consisting of crystals with a low or almost random crystal co-orientation strength (e.g. [32,50]). This is observed, for example, for the shell of thecideid brachiopods [55] and for the shell of the bivalve *Arctica islandica* (Linnaeus, 1767) [56], the latter being a species having a marked longevity and, thus, slow shell secretion, even though it forms its shell out of only one microstructure and a very low crystal co-orientation strength [56]. Based on crystal co-orientation strength, it cannot be determined if the mineralized components of the shell are precipitated from seawater or are secreted biologically. We consider the cementation granules as well as the calcite of the rest of the Ostreoidea shell as being the product of biological secretion.

The myostracal layers

The myostraca of bivalves are always formed of aragonite, even if the rest of the shell consists of calcite (e.g. [41,57] and references therein, [58]). This is not the case for all bivalved marine organisms. E. g. brachiopod myotests, the scars of the brachiopod muscle attachment sites, consist of calcite [59,60]. Modern rhynchonelliform brachiopods secrete calcitic shells as well as calcitic muscle scars [60].

In the case of Ostreoidea, not only the carbonate phase of their myostraca is different to the mineralogy of the rest of the shell, all other structural attributes of their myostraca are different as well, e.g., crystal morphology, crystal co-orientation strength, myostracal microstructure and texture (Fig. 9). The marked difference in structure, microstructure and texture of the myostracum and of the rest of the shell is the result of the influence of determinants that affect the formation of the different microstructures. The columnar, foliated, and granular microstructures of Ostreoidea shells are mainly the result of biological determinants, while the myostracal microstructure, even though secreted by an organism, is mainly influenced by physical crystal growth determinants. Physical determinants do not exert influence on the growth of columnar, foliated and the cementation crystals. For further information on biological hard tissue formation determinants see Checa [22]; for physical determinants of myostracal crystal growth see Hoerl et al. [41,57].

The crystal growth process of Ostreoidea myostracal crystals is the process of growth competition. At the latter growth process, the orientation of the crystal's growth axis, for calcite the c-axis, determines the success of a crystal to grow to a large entity. Myostracal crystals nucleate onto the adjacent shell layer template, in the case of the Ostreoidea, onto the foliated shell template. The first crystals that form are minute and have random orientation [17,28,30]. As crystal nucleation occurs at high supersaturation, many crystals nucleate next to each other and, with growth, compete for space. Those crystals that have their fastest growth axis oriented perpendicular to the orientation of the template surface, thus, perpendicular to the foliated layer surface, can grow without any inhibition and develop to large crystal entities. Crystals that have their fastest growth axis direction

 doi:10.20944/preprints202502.0108.v1

at an angle to the nucleation template, to the surface of the foliated shell layer, collide at growth with their neighbors and, due to restriction in available space, become eliminated. Hence, due to the growth process, the inner myostracal shell surface is seamed by large myostracal prisms and the c-axis of adjacent prisms is parallel to each other and is oriented normal to inner shell surface.

Our EBSD results show a further important structural characteristic for the myostracal microstructure of the investigated Ostreoidea shells. Myostracal aragonite is twinned (see the marked misorientation peaks at 63°/64° in the misorientation diagrams in in Fig. 9C, G), while columnar, foliated, granular, chalk, rhombohedral calcite of the investigated Ostreoidea shells in not twinned. The lack of crystal twinning of Ostreoidea calcite will be discussed subsequently.

3.2. The microstructures that enable the incorporation of voids into the shells

The Ostreoidea developed two strategies for enabling cavity incorporation into the shell. Ostreidae incorporate voids into the foliated shell layer with the inclusion of the chalk lenses (Figs. 10, 11 [17,28,30,61]). The Gryphaeidae generate a shell layer with a specific vesicular microstructure that allows the incorporation of large sequences of pores into that layer (Figs. 12, 13 and [1,12,62,63]). The shell layer that hosts the vesicular pores is never within the foliated microstructure, nonetheless, always associated to it. The chalk and the vesicular microstructures are considered to be structurally unrelated [12,28]). This is an indication that the Ostreidae and the Gryphaeidae arrived independently to a comparable Ca-carbonate material functionalization solution that, most probably, was and is driven by adaptation to similar environmental requirements. The foliated microstructure plays an important role in facilitating void and pore incorporation, as both the void-rich chalk lenses as well as the arrays of the vesicular pores are in topological relation to the foliated mode of crystal and crystal unit arrangement, and are not in structural relation to other crystal, crystal unit arrangements, e.g., to the columnar assembly of crystals.

The structure of the meshwork of chalk blades and laths is very specific. In particular, when the degree of structuring is considered, it is very different to the arrangement of folia that surrounds the chalk lenses. The observation of these differences led to the suggestion that the blades/laths and the foliae are formed through different biomineralization processes. Chinzei and Seilacher [64], Vermeij [65] and Banker and Vermeij [66] suggested that sulfur reducing bacteria, living within the shell, could be responsible for the formation of chalk blade calcite and, as calcite formation by bacteria is a precipitation process, bacterial precipitation might be responsible for the specific microstructure of the chalk. This concept was challenged by Korringa [67], Pelseneer [68], Ranson [63], Galtsoff [69], Margolis and Carver [70], Ullmann et al. [71], Checa et al. [28], Banker and Sumner [31] and de Winter et al. [72]. The studies of the latter authors indicate that the chalk as well as all other oyster shell layers are deposited directly by the oyster. In addition, in favor of the latter is the similarity in isotopic signature of chalk and foliated calcite [71,72]. A possible explanation for the specific microstructure of the chalk and the disordered structural nature of chalk blades/laths was given by Checa et al. [28]. The authors suggested that the foliated layer and the chalk lenses grow at different rates; the cavity-rich chalk calcite is formed at a higher thickening speed, relative to the thickening speed of the dense foliated material.

SEM images of the chalk structure convey the impression that the chalk is a fully random assembly of blades and laths (e.g. Fig. 10A, B and see MUD values for the chalk in Fig. 10E, F). However, EBSD scans taken on the chalk show some internal structuring (Fig. 11D). The aggregation of the laths is pervaded by undulated blades (Fig. 11D), possibly for the stabilization of the cavity-rich chalk structure. Individual chalk blades have an increased to, even, high crystal co-orientation strengths (Tab. 1) and traverse the chalk structure over large distances (Fig. 11D, E). Thus, one can find for EBSD scans, performed on the chalk, also high crystal co-orientation strengths (e.g., an MUD of 45; Fig. 11D or 24; Fig. 11E). Furthermore, we see in misorientation angle diagrams for all EBSD scans conducted on the chalk, the tendency to formation of large misorientations. This indicates some structural organization of the chalk microstructure as well.

 doi:10.20944/preprints202502.0108.v1

The Gryphaeidae developed a different strategy for the incorporation of cavities into their shell. Gryphaeidae secrete a shell layer with a specific microstructure, which is capable to accommodate for the incorporation of large sequences of vesicular pores. The latter is possible through the interlinkage of crystals having highly irregular and strongly fractal morphologies (Fig. 12D). These crystals are dendritic, interlink strongly in 3D (see the dendritic crystal and its neighbors in Fig. 13B) and form a microstructure that has also a very low crystal co-orientation strength (Table 1). The pores are, in general, large-sized cavities (Figs. 12, 13), thus, the mineralized structure that encases the pores needs to be particularly robust. This is realized by the Gryphaeidae with a shell layer structure consisting of crystals with very fractal shapes (Figs. 12D, 13) and a pronounced, but, in 3D, variously oriented, interlinkage of the dendritic crystals (Figs. 12B, D, 13B, EBSD map for dendritic crystals in Fig. 14A). As it is the case for the columnar and the foliated shell layers, for the dendritic crystal shell layer as well, we find that crystal units are formed of strongly co-oriented calcite (see MUD values of individual crystals in Fig. 13C), while the respective shell layer has a low crystal co-orientation strength (Table 1).

Gryphaeidae are not the only bivalved organisms that secrete a meshwork of fractal crystals for shell formation. We find a similar microstructural motif, rooted in the interlinkage of strongly fractal-shaped calcite crystals, for the formation of the primary shell layer by modern rhynchonelliform brachiopods (Figs. 19A to C, 20A in [55]). A tight interlinkage of fractal-shaped calcite crystals generates the microstructure of modern thecideid brachiopod shells (Fig. 10 in [73]) and the ornamentation microstructure of the modern venerid bivalve *Chama arcana* (Fig. 3b, c in [57]). For the formation of the gryphaeid dendritic microstructure, the pronounced fractality of the crystals is very essential. This facilitates their tight interlinkage in 3D as well as an undirected mode of interlinkage and enables the formation of a dense, strong and tough microstructure. It should be noted that all above given examples for shell layer formation out of interlinked, fractal-shaped, dendritic crystals are calcitic microstructures. To the knowledge of the authors, this microstructural motif has not been observed yet for biologically formed aragonites.

3.3. Formation of curved surface with Ostreoidea shell crystals

For the investigated Ostreoidea shells we see the development of curved surfaces. These are present at inner shell surface, for both the Ostreidae and Gryphaeidae. For the Gryphaeidae, in addition, we find curved surfaces also within the shell, the inner surface of the pores, present in the shell layer formed by the fractal-shaped crystals.

When a curved *inner shell surface* is generated by the Ostreoidea, the size of the foliated units decreases towards the inner shell surface (Figs. 8, S4). Thus, an Ostreoidea inner shell surface that is curved is seamed by small foliated units. In addition, as the difference in point to point misorientation between the foliated units shows (Fig. 5B, C), the degree of misorientation between adjacent folia, for a foliated unit, decreases towards inner shell surface. Thus, at Ostreoidea inner shell surface a microstructure is present with small foliated units and with the comprising folia having a low crystal co-orientation strength. See the difference in microstructure between sections a and b of the EBSD scan given in Fig. 8. We can observe well that the shell layer section formed of small foliated units does not abruptly change into a shell portion with large foliated units. The change from large to small foliated units is gradual (Fig. 8B).

Curved surfaces forming the *inner surface of the pores* of the Gryphaeidae (Figs. 12E, 13) are generated with formation of a shell layer consisting of strongly interlinked, little co-oriented, fractal-shaped crystals. Thus, the main difference in structural strategy of curved surface formation between Ostreidae and Gryphaeidae lies in crystal shape.

3.4. The textures

We described in the Results section and discussed in the Discussion section the large diversity of crystal morphologies and the diversity of microstructures that oysters can generate with the crystals they secrete. Do we find such a diversity in crystal textures?

 doi:10.20944/preprints202502.0108.v1

As the pole figures in Figs. 3H, I, 7B to D, 9C, E, 10F, 11A, B, 12A, 13, 14B demonstrate, Ostreoidea are capable to secrete calcite with diverse texture modes and this in the same shell. Within the same oyster shell, we find single crystal-like textures (individual columns, individual foliated units), axial textures (columnar layer), turbostratic-like textures (foliated layer) and polycrystalline textures with an almost random preferred orientation of the crystals (meshwork of the chalk, layer formed by dendritic crystals, cementation layer). Thus, we find within an Ostreoidea shell all main texture patterns that are observed today for Ca-carbonate microstructures secreted by marine organisms (Fig. 12.15 in [32], [87].

In essence, our study shows for the texture of Ostreoidea Ca-carbonate shells that (i) the diversity of texture patterns in Ostreoidea shells is increased, relative to the diversity of texture patterns that we detect for the shells of other bivalved, biocarbonate-forming, marine organisms (bivalves as well as brachiopods). (ii) we observe for Ostreoidea shells a larger diversity in crystal microstructures, relative to what we find for the crystal textures.

3.5. The change from one microstructure into the other

As Ostreoidea shells are formed of calcite, disregarding the few patches of myostracal and ligament aragonite, and as their shell comprises many microstructure patterns, Ostreoidea shells are ideal for the investigation of structural features at the changeover from the one microstructure into the other. We investigated the latter from a crystallographic point of view and discuss, subsequently, some crystallographic characteristics of calcite crystals that we observe for the different microstructure changeovers (Figs. 15 to 18). We show crystal orientation that prevails at the interface between adjacent microstructures with the corresponding EBSD maps, but also with the {100} (a*-axes), <001> (c-axes) and the {104}, {018}, {012} pole figures. These pole figures are shown for the one microstructure, e.g., for the columns, as well as for the latter, the adjacent microstructure, e.g., the columns and the folia. For a better visualization of the nature of the changeover, we complement the EBSD scans and pole figures with relative frequency–misorientation angle diagrams (Figs. 16, 17).

3.5.1. Crystal rotation

For the changeover from foliated to columnar crystals, we observe a steady rotation of crystallographic axes between the columns and the folia (Fig. 15A to E). See in the pole figure the gradedness in c- and a*-axes for a calcite unit/entity comprising a column and the adjacent stack of folia (Fig. 15E).

 doi:10.20944/preprints202502.0108.v1

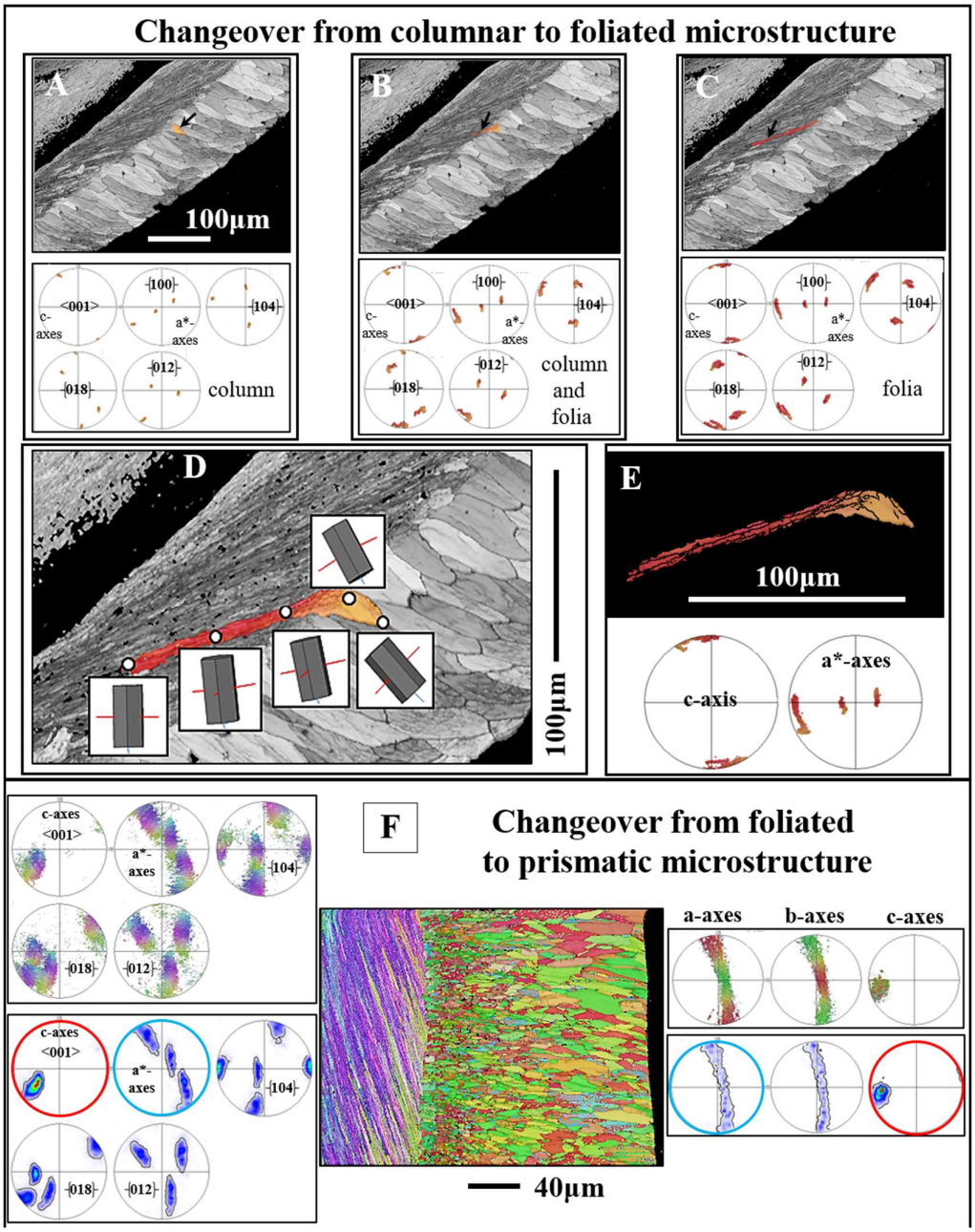

Figure 15. Calcite c- and a*-axes orientations at the changeover from columns to the stacks of folia (A to E) and from the assembly of folia to myostracal prisms (F). For investigation of a possible crystal twin-related change between adjacent microstructures, we show, in addition to the c-axis (the {001} pole figure) and a*-axes (the {110} pole figure) orientations, pole figures for {104}, {018} and {012} plane orientations. As it is well visible from the pole figures in Fig. 15A to C, the transition from the columns to the adjacent folia is not twin operation related. It is rather a gradual, crystal rotation-based, change between the crystallites of the columnar to the crystallites of the foliated shell layers (D, E). F: Changeover from foliated calcite to myostracal, prismatic, aragonite. Even though the microstructures, as well as the textures, are very different for these two shell layers, we find some correspondence in c-axes orientation (see pole figures encircled in red in F) and some correspondence in a*-axes orientations for the calcite and the aragonite (see the pole figures encircled in blue in F). At EBSD data acquisition and EBSD data evaluation, the three Euler angles were kept at 0°; $\phi1$=0°, Φ=0°, $\phi2$=0°. A to E: *Magallana gigas*. F: *Ostrea stentina*.

 doi:10.20944/preprints202502.0108.v1

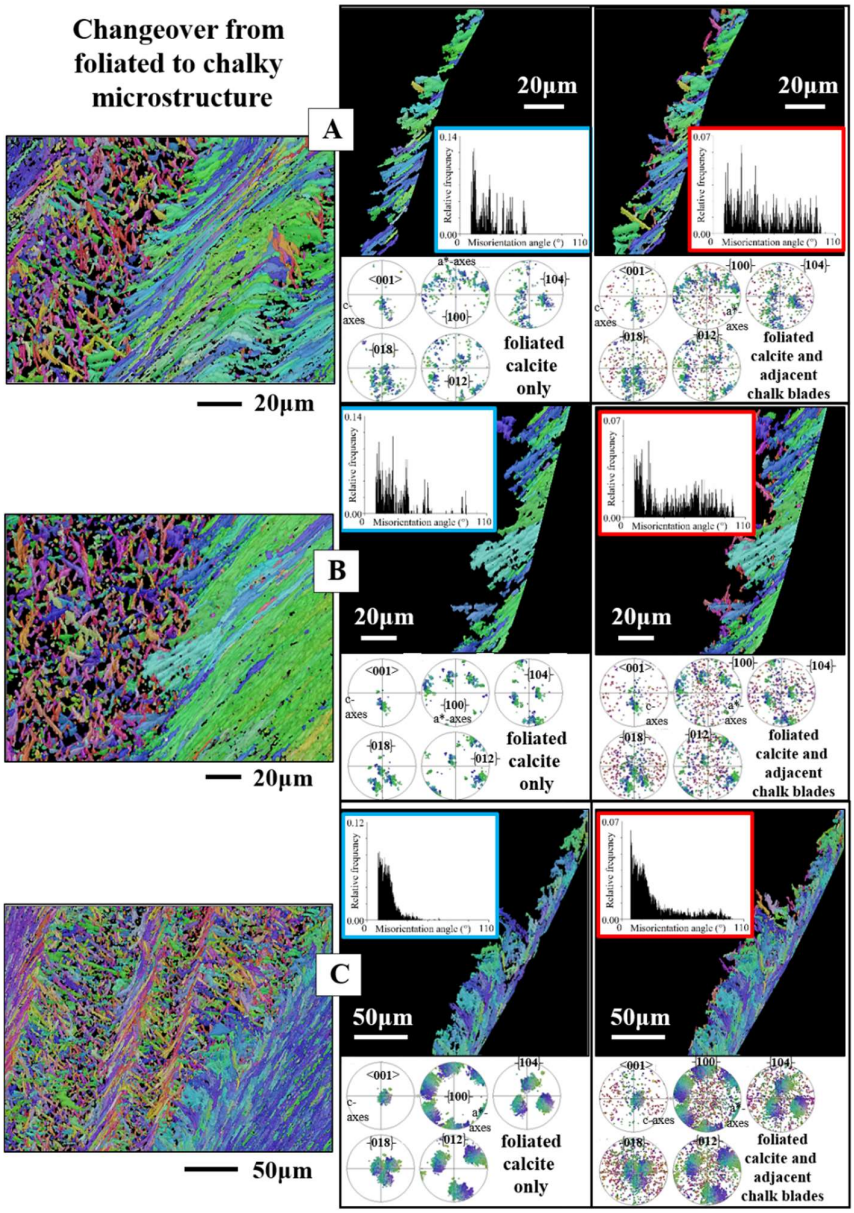

Figure 16. EBSD scans, color-coded for crystal orientation, visualize calcite c- and a*-axes orientation at the changeover from foliated to chalky calcite (A to C). We show with pole figures c-axis ({001} pole figure) and a*-axes ({100} pole figure) as well as the {104, {018} and {012} orientations. These are shown for (i) only the foliated calcite and (ii) for the foliated calcite and the, to the calcite attaching, chalk blades. In addition, we give corresponding relative frequency-misorientation angle diagrams for the crystal orientations given in A to C. We do not find a crystal twin-related changeover from foliated to chalk calcite. If the latter was the case, we would need to observe in the misorientation angle diagrams for the folia and the directly adjacent chalk crystals a marked peak in either 60°, 78.1°, 78.8° and 104° misorientation, as defined according to the twin laws of calcite [42, 43]. We demonstrate with the absence of a marked peak at 60°, 78°/79° and 104° misorientation and the {001}, {104, {018} and {012} pole figures that foliated and chalk calcite are not twinned and that the changeover from folia to chalk calcite is not given with a calcite twin related crystallographic operation. At EBSD data acquisition and EBSD data evaluation, the three Euler angles were kept at 0°; ϕ1=0°, Φ=0°, ϕ2=0°. A to F: *Magallana gigas*.

 doi:10.20944/preprints202502.0108.v1

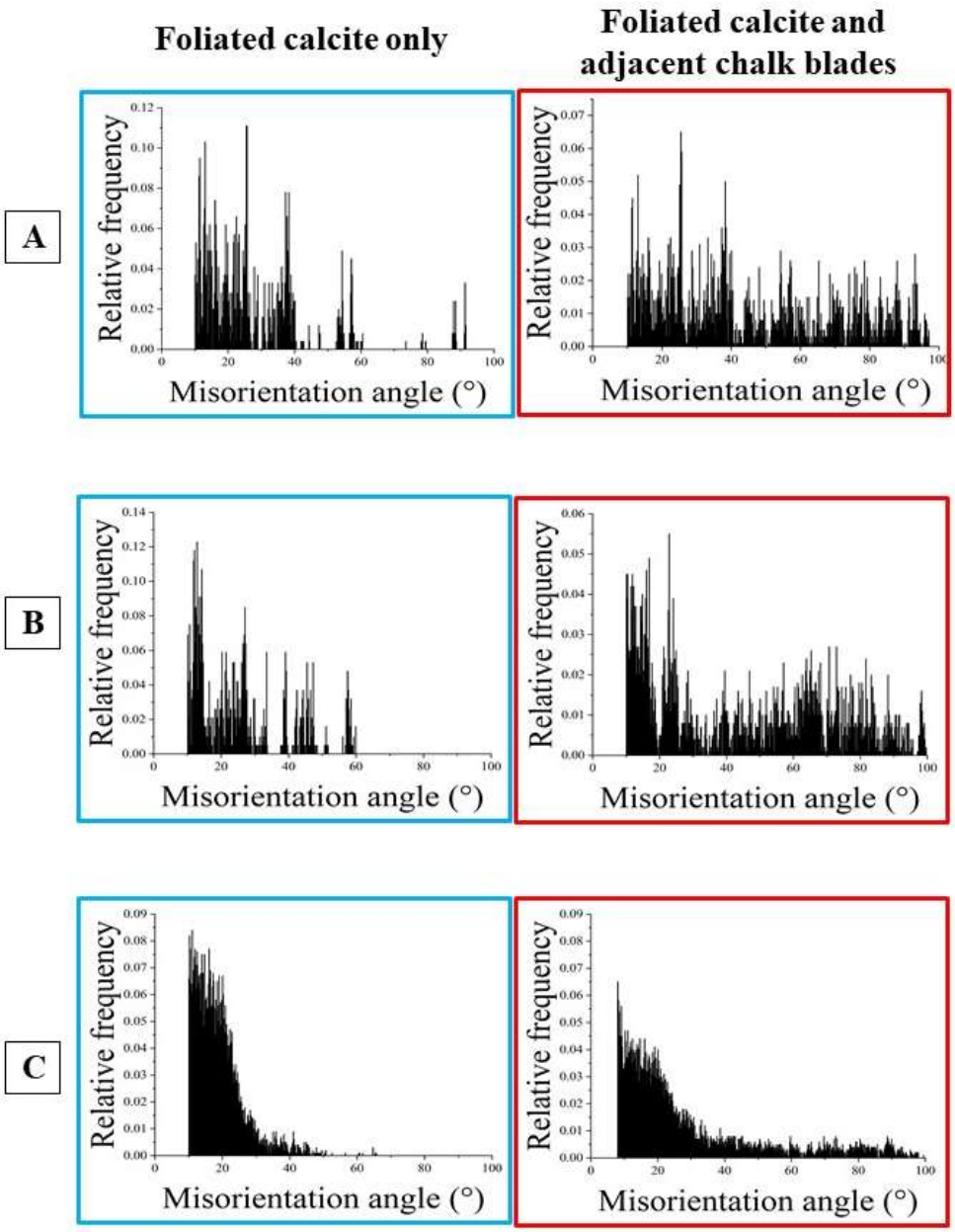

Figure 17. Enlargement of the relative frequency-misorientation angle diagrams shown in Fig. 16. Framed in blue are misorientation angle diagrams for only the folia, framed in red are misorientation angle diagrams for the folia and the adjacent, directly touching, chalk blades. We do not observe a marked peak at 60°, 78.1, 78.8°, 104° misorientation. This demonstrates the absence of a calcite twin operation-related structural change from the foliated into the chalk microstructure. A to F: *Magallana gigas*.

 doi:10.20944/preprints202502.0108.v1

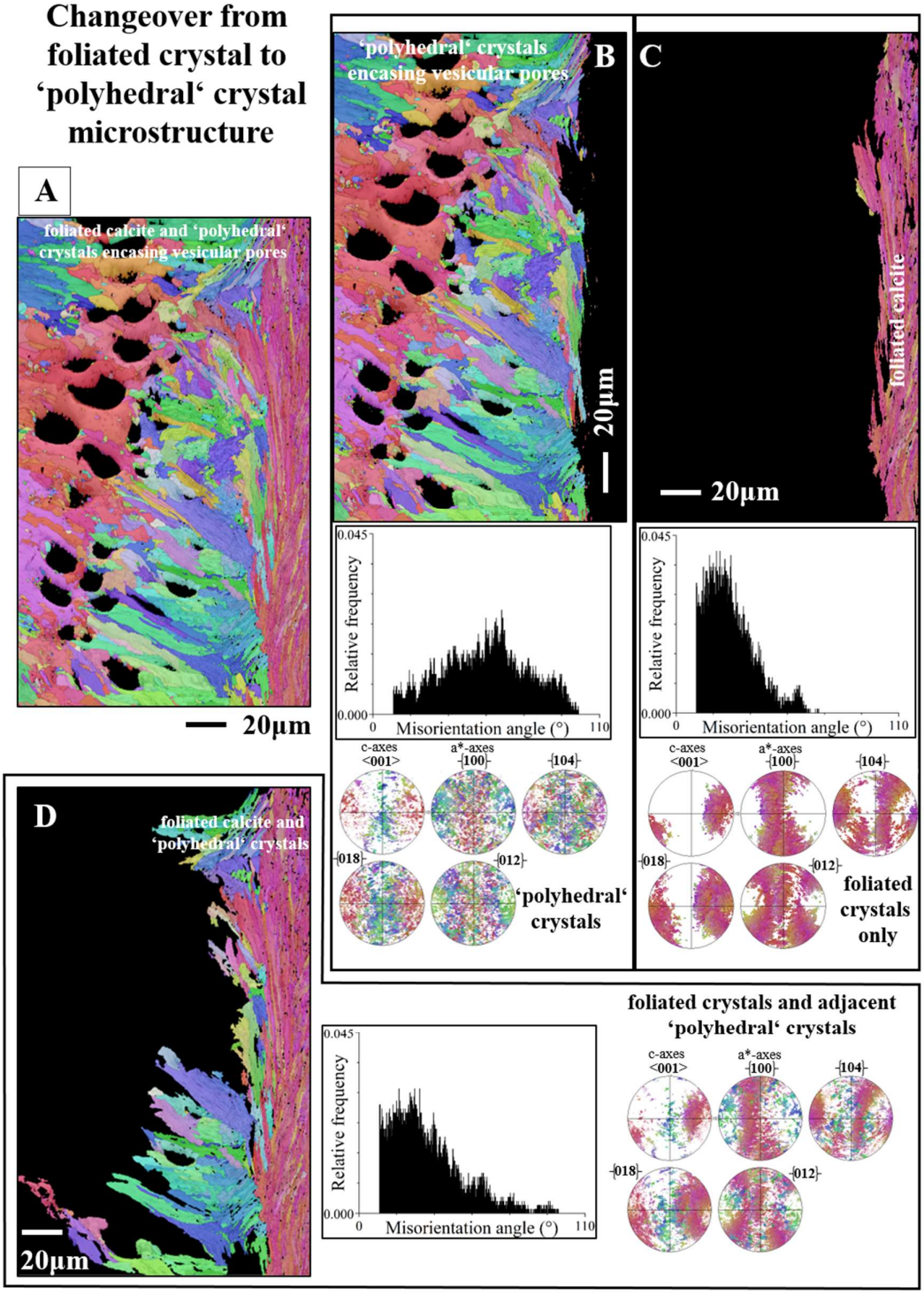

Figure 18. The changeover from foliated to 'dendritic' calcite (A, D). The change from one microstructure into the other is rather abrupt. For the foliated and the adjacent dendritic, polyhedral, crystals (D) we do not find a marked peak at 60°, 78.1, 78.8°, 104° in the relative frequency-misorientation angle diagram (D), nor any indication of twin formation in the (001), (104), (018), (012) pole figures (D). This indicates that the changeover from the foliated to the 'dendritic' crystal shell portion is not the result of a calcite twin-related crystallographic operation. At EBSD data acquisition and EBSD data evaluation, the three Euler angles were kept at 0°; ϕ1=0°, Φ=0°, ϕ2=0°. A to D: *Neopycnodonte cochlear*.

 doi:10.20944/preprints202502.0108.v1

3.5.2. Oriented nucleation

The changeover from foliated calcite to prismatic aragonite can be addressed as the oriented nucleation of myostracal prisms onto the foliated crystals (Fig. 15F). Even though we find significant differences in texture for the folia and the myostracal prisms, as c-axes orientation of an assembly of foliated units has a ring-shaped distribution, there will always be c-axes orientations of some foliated units that are parallel to the c-axes orientation of myostracal prism aragonite. However, due to the difference in foliated and myostracal-prismatic texture, there is no correspondence between the foliated calcite and the myostracal aragonite a*- (calcite) and a- (aragonite) axes orientation (Fig. 15F). For further discussion of the latter, see Griesshaber et al. [50].

3.5.3. Crystal twin-related changeover

From foliated crystals to chalk blades

Due to the large spread in crystallographic axes orientation of chalk calcite (e.g. the pole figure for chalk calcite in Fig. 10F), it is difficult to describe the changeover from foliated to chalk calcite, as the wide spread in chalk crystal orientation masks the nature of the changeover. Nonetheless, based on misorientation diagrams and on the pole figures for the four twin laws of calcite (Figs. 16, 17) we can determine whether there is a crystal twin-related relationship between the folia and the chalk blades/laths, thus, a twin-related changeover from the foliated layer to the chalk lens.

A twined crystal is an intergrowth of two or more crystal domains of the same phase and chemical composition [74]. The twin domains have different orientations. Their orientational relationship, however, is crystallographically defined through a mirror operation on a crystallographic lattice plane or a rotation around a crystallographic axis. Thus, the domains of a twinned crystal are related to each other through crystallographically defined misorientations; the degree of the twin-related misorientation is defined by the twin law. As twin crystals are intergrowths of domains, for the proof of a crystal twin-based relation between crystals, it is necessary to examine directly adjacent crystals, thus, to examine a possible twin formation for a folium or a foliated unit that is directly adjacent to a chalk blade or to a cluster of chalk blades. This is the case for the examples that we show in Fig. 16A to C. We give three EBSD scans misorientation angle diagrams and twin law-related pole figures for (i) only the foliated calcite and (ii) for the foliated calcite and the directly adjacent chalk blades.

The mode of intergrowth of twin domains is defined by the twin laws [74]. Inorganic calcite is known to follow four classical twin laws, named after the Miller indices of the twin planes, the {104}, {018}, {012} and {001} planes [74,75]. These twin laws are regarded as the classical twin laws of calcite. Yin et al. [76], Lastam et al. [77] and Lastam et al. [78] showed that the most frequently occurring biocalcite twin law is the {001} twin. Pokroy et al. [79] identified a fifth {108} twin in biogenic calcite. Schmahl et al. [80] detected, also for biologically secreted calcite, a further systematically and frequently reoccurring misorientation, a misorientation of 78° on the [6 -6 1] twin axis and addresses this misorientation as a non-classical form of calcite twinning. Accordingly, when the changeover from folia to chalk blades is determined by a twin-related crystallographic operation, we need to see this not only in the pole figure given for the relevant twin, but also and, in particular, we need to see a marked peak in the misorientation angle diagram at a specific misorientation, which is defined by the relevant twin law. In the case of crystal twinning at the changeover from foliated to bladed calcite we should see a peak either at 60°, 78°, 79° or/and 104° misorientation. For the EBSD measurements, covering the foliated and adjacent chalk calcite, we find neither in the pole figures nor in the corresponding misorientation angle diagrams any indication for a twin-related changeover from the folia to the chalk blades (Figs. 14, 15).

The structural relationship between adjacent columns

The EBSD scans that were measured for this study allowed the investigation of the mode of misorientation between adjacent columns of the Ostreoidea columnar shell layer, in particular, the structural analysis if adjacent columns are related to each other by a twin-related orientation relationship. As the orientational relationship of the twin domains of a twin crystal is

 doi:10.20944/preprints202502.0108.v1

crystallographically defined and is either a mirror operation on a crystallographic lattice plane or a rotation around a crystallographic axis, we show, for a large array of columns:

1. along trajectories A to B (i) relative frequency–misorientation angle diagrams and (ii) degree of misorientation–distance diagrams (Fig. S6).
2. In addition, we give for 67 trajectories taken on adjacent columns (Fig. S7A): (i) the misorientation angles and their frequencies (Fig. S7B) as well as (ii) the crystallographic indices of the misorientation axes and the frequencies of these misorientation axes (Fig. S7C).

Thus, if adjacent columns are related to each other through a crystal twin-defined orientational relationship, we would need to see a specific calcite twin law-related misorientation (at 60°, 78°, 79° or/and 104° misorientation) in one of the misorientation diagrams (Fig. S6) or a frequently occurring, calcite twin law-related angle (Fig. S7B, C), or a frequently occurring, twin law-related crystallographic axis, preferentially the (001) axis (Fig. S7C). None of these is the case. We neither see a marked peak at (at 60°, 78°, 79° or/and 104° misorientation) in one of the misorientation diagrams, nor an often occurring, calcite twin-related, misorientation angle (Fig. S7B), nor the frequent presence of a crystallographic axis (Fig. S7C, D).

In essence, we examined in great detail calcite and aragonite crystal twin generation for the different shell microstructures of the investigated Ostreoidea species. For none of the calcite structures did we find any twin formation, only for myostracal aragonite. Crystal twin formation is widely observed for biological aragonites, e.g. for bivalves, gastropods, otoliths, corals [81,82], for bivalve columnar [81,83] and sheeted [81,82,84] nacre, for bivalve complex and crossed-lamellar aragonite [41,57,60,81,82,85–88] and for bivalve myostracal aragonite [41,57,60]. In contrast, disregarding the calcite of rotaliid foraminifera shells [76,78], crystal twin formation is absent in biologically secreted calcite. This is very surprising; we do not know the reason for that and need to decipher in future this structural imbalance.

Author Contributions:A.S.V. worte the manuscript and evaluated the EBSD data, E.G. performed EBSD measurements and evaluated the EBSD data, A.G.C. discussed the EBSD data and wrote the manuscript, W.W.S. discussed the EBSD data and wrote the manuscript, C.S. and E.M.H. discussed EBSD data and helped with writing the manuscript.

Data Availability Statement: The raw data supporting the conclusions of this article will be made available by the authors on request.

Acknowledgements: We thank Sebastian Hoerl for evaluating many EBSD data sets also with AZTec Crystal and for his comments to the manuscript. We thank Lisa Kreitmeier for the preparation of some Ostreoidea samples. W.W.S., E.G. and A.S.V. acknowledge funding by the German Research Council Programmes GR 9/1234, SCHM 930/11-2. A.G.C., and C.S.C acknowledge funding by projects PID2023-146394NB-I00 and PID2020116660GB-I00 (Spanish Ministry of Science and Innovation: MCIN/AEI/10.13039/501100011033/). A.G.C. also acknowledges the Unidad Científica de Excelencia UCE-PP2016-05 (University of Granada) and the Research Group RNM363 (Junta de Andalucía).

Conflicts of Interest: The authors declare no conflict of interest.

 doi:10.20944/preprints202502.0108.v1

References

1. Stenzel, H.B. Systematic Descriptions. In *Treatise on invertebrate paleontology: Part N Mollusca 6: Bivalvia: Oysters*; Moore, R.C., Ed.; The Geological Society of America: Boulder, CO, U.S.A., 1971; Vol. 3, pp. 1096–1172 ISBN ISBN 0-8137-3026-0.
2. Márquez-Aliaga, A.; Jiménez-Jiménez, A.P.; Checa, A.G.; Hagdorn, H. Early Oysters and Their Supposed Permian Ancestors. *Palaeogeogr. Palaeoclimatol. Palaeoecol.* **2005**, *229*, 127–136, doi:10.1016/j.palaeo.2005.06.034.
3. Mouchi, V.; Pecheyran, C.; Claverie, F.; Cathalot, C.; Matabos, M.; Germain, Y.; Rouxel, O.; Jollivet, D.; Broquet, T.; Comtet, T. A Step towards Measuring Connectivity in the Deep Sea: Elemental Fingerprints of Mollusk Larval Shells Discriminate Hydrothermal Vent Sites. *Biogeosciences* **2024**, *21*, 145–160, doi:10.5194/bg-21-145-2024.
4. Yonge, C.M. *Oysters*; Collins, 1960;
5. Bricteux-Gregoire, S.; Duchateau-Bosson, G.; Jeuniaux, C.; Florkin, M. Constituants Osmotiquement Actifs Des Muscles Adducteurs d'ostbea Edulis Adaptée a L'eau de Mer Ou a L'eau Saumatre. *Arch. Int. Physiol. Biochim.* **1964**, doi:10.3109/13813456409058972.
6. Van Rooij, D.; De Mol, L.; Le Guilloux, E.; Wisshak, M.; Huvenne, V. a. I.; Moeremans, R.; Henriet, J. Environmental Setting of Deep-Water Oysters in the Bay of Biscay. *DEEP-SEA Res. PART -Oceanogr. Res. Pap.* **2010**, *57*, 1561–1572, doi:10.1016/j.dsr.2010.09.002.
7. Bieler, R.; Mikkelsen, P.M.; Lee, T.; Foighil, D.Ó. Discovery of the Indo-Pacific Oyster *Hyotissa Hyotis* (Linnaeus, 1758) in the Florida Keys (Bivalvia : Gryphaeidae). *Molluscan Res.* **2004**, *24*, 149–159, doi:10.1071/mr04013.
8. Nakahara, H.; Bevelander, G. The Formation and Growth of the Prismatic Layer of *Pinctada Radiata*. *Calcif Tissue Res* **1971**, *7*, 31–45.
9. MacDonald, J.; Freer, A.; Cusack, M. Alignment of Crystallographic C-Axis throughout the Four Distinct Microstructural Layers of the Oyster *Crassostrea Gigas*. *Cryst. Growth Des.* **2010**, *10*, 1243–1246, doi:10.1021/cg901263p.
10. Dauphin, Y.; Ball, A.D.; Castillo-Michel, H.; Chevallard, C.; Cuif, J.-P.; Farre, B.; Pouvreau, S.; Salomé, M. *In Situ* Distribution and Characterization of the Organic Content of the Oyster Shell *Crassostrea Gigas* (Mollusca, Bivalvia). *Micron* **2013**, *44*, 373–383, doi:10.1016/j.micron.2012.09.002.
11. Checa, A.G.; Macías-Sánchez, E.; Harper, E.M.; Cartwright, J.H.E. Organic Membranes Determine the Pattern of the Columnar Prismatic Layer of Mollusc Shells. *Proc R Soc B* **2016**, *283*.
12. Checa, A.G.; Linares, F.; Maldonado-Valderrama, J.; Harper, E.M. Foamy Oysters: Vesicular Microstructure Production in the Gryphaeidae via Emulsification. *J. R. Soc. Interface* **2020**, *17*, 20200505, doi:10.1098/rsif.2020.0505.
13. Sancho Vaquer, A.; Checa, A.G.; Griesshaber, E.; Fernandez-Diaz, L.; Salas, C.; Schmahl, W.W. Layers Formed of Rhombohedral Calcite and Biopolymers in Oyster Shells. *Crystals* 2025, *submitted*.
14. Liu, J.; Li, Q.; Kong, L.; Yu, H.; Zheng, X. Identifying the True Oysters (Bivalvia: Ostreidae) with Mitochondrial Phylogeny and Distance-Based DNA Barcoding. *Mol. Ecol. Resour.* **2011**, *11*, 820–830, doi:10.1111/j.1755-0998.2011.03025.x.
15. Bai, Y.; Liu, S.; Hu, Y.; Yu, H.; Kong, L.; Xu, C.; Li, Q. Multi-Omic Insights into the Formation and Evolution of a Novel Shell Microstructure in Oysters. *BMC Biol.* **2023**, *21*, 204, doi:10.1186/s12915-023-01706-y.
16. Taylor, J.D.; Kennedy, W.J.; Hall, A. The Shell Structure and Mineralogy of the Bivalvia Introduction. Nuculacea-Trigonacea. *Bull Br Mus Nat Hist* **1969**, *Suppl. 3*, 1–125.
17. Carriker, M.R.; Palmer, R.E.; Sick, L.V.; Johnson, C.C. Interaction of Mineral Elements in Sea Water and Shell of Oysters (*Crassostrea Virginica* (Gmelin)) Cultured in Controlled and Natural Systems. *J. Exp. Mar. Biol. Ecol.* **1980**, *46*, 279–296, doi:10.1016/0022-0981(80)90036-2.
18. Dungan, C.F. Aragonite-Fiber Calcification of the Hinge Ligament Mechanical Antagonist to Valve Adduction in Oysters. In Proceedings of the Journal of Shellfish Research; National Shellfisheries Association: Providence, Rhode Island, 2008; Vol. 27, pp. 1004–1005.
19. Mouchi, V.; Lartaud, F.; Guichard, N.; Immel, F.; de Rafélis, M.; Broussard, C.; Crowley, Q.G.; Marin, F. Chalky versus Foliated: A Discriminant Immunogold Labelling of Shell Microstructures in the Edible Oyster *Crassostrea Gigas*. *Mar. Biol.* **2016**, *163*, 256, doi:10.1007/s00227-016-3040-6.
20. Runnegar, B. Crystallography of the Foliated Calcite Shell Layers of Bivalve Molluscs. *Alcheringa Australas. J. Palaeontol.* **1984**, *8*, 273–290, doi:10.1080/03115518408618949.

21. Checa, A.G.; Esteban-Delgado, F.J.; Rodríguez-Navarro, A.B. Crystallographic Structure of the Foliated Calcite of Bivalves. *J. Struct. Biol.* **2007**, *157*, 393–402, doi:10.1016/j.jsb.2006.09.005.
22. Checa, A.G. Physical and Biological Determinants of the Fabrication of Molluscan Shell Microstructures. *Front. Mar. Sci.* **2018**, *5*.
23. Esteban-Delgado, F.J.; Harper, E.M.; Checa, A.G.; Rodríguez-Navarro, A.B. Origin and Expansion of Foliated Microstructure in Pteriomorph Bivalves. *Biol. Bull.* **2008**, *214*, 153–165, doi:10.2307/25066672.
24. Checa, A.G.; Esteban-Delgado, F.J.; Ramírez-Rico, J.; Rodríguez-Navarro, A.B. Crystallographic Reorganization of the Calcitic Prismatic Layer of Oysters. *J. Struct. Biol.* **2009**, *167*, 261–270, doi:10.1016/j.jsb.2009.06.009.
25. Harper, E.M. Post-Larval Cementation in the Ostreidae and Its Implications for Other Cementing Bivalvia. *J. Molluscan Stud.* **1992**, *58*, 37–47, doi:10.1093/mollus/58.1.37.
26. Harper, E.M. Attachment of Mature Oysters (*Saccostrea Cucullata*) to Natural Substrata. *Mar. Biol.* **1997**, *127*, 449–453, doi:10.1007/s002270050032.
27. MacDonald, J.; Freer, A.; Cusack, M. Attachment of Oysters to Natural Substrata by Biologically Induced Marine Carbonate Cement. *Mar. Biol.* **2010**, *157*, 2087–2095, doi:10.1007/s00227-010-1476-7.
28. Checa, A.G.; Harper, E.M.; González-Segura, A. Structure and Crystallography of Foliated and Chalk Shell Microstructures of the Oyster *Magallana*: The Same Materials Grown under Different Conditions. *Sci. Rep.* **2018**, *8*, 7507, doi:10.1038/s41598-018-25923-6.
29. Bayne, B.L. *Biology of Oysters*; 1st Edition.; Academic Press: London, 2017; Vol. 41; ISBN 978-0-12-803472-9.
30. Higuera-Ruiz, R.; Elorza, J. Biometric, Microstructural, and High-Resolution Trace Element Studies in *Crassostrea Gigas* of Cantabria (Bay of Biscay, Spain): Anthropogenic and Seasonal Influences. *Estuar. Coast. Shelf Sci.* **2009**, *82*, 201–213, doi:10.1016/j.ecss.2009.01.001.
31. Banker, R.M.W.; Sumner, D.Y. Structure and Distribution of Chalky Deposits in the Pacific Oyster Using X-Ray Computed Tomography (CT). *Sci. Rep.* **2020**, *10*, 12118, doi:10.1038/s41598-020-68726-4.
32. Griesshaber, E.; Yin, X.; Ziegler, A.; Kelm, K.; Checa, A.; Eisenhauer, A.; Schmahl, W.W. Patterns of Mineral Organization in Carbonate Biological Hard Materials. In *Highlights in Applied Mineralogy*; Heuss-Aßbichler, S., Amthauer, G., John, M., Eds.; De Gruyter, 2017; pp. 245–272 ISBN 978-3-11-049734-2.
33. Hedegaard, C.; Wenk, H.-R. Microstructure and Texture Patterns of Molluse Shells. *J. Molluscan Stud.* **1998**, *64*, 133–136, doi:10.1093/mollus/64.1.133.
34. Chateigner, D.; Hedegaard, C.; Wenk, H.-R. Mollusc Shell Microstructures and Crystallographic Textures. *J. Struct. Geol.* **2000**, *22*, 1723–1735, doi:10.1016/S0191-8141(00)00088-2.
35. Hull, D. *Introduction to Dislocations*; Pergamon Press GmbH: Kronberg-Taunus, 1975;
36. Seto, J.; Ma, Y.; Davis, S.A.; Meldrum, F.; Gourrier, A.; Kim, Y.Y.; Schilde, U.; Sztucki, M.; Burghammer, M.; Maltsev, S.; et al. Structure-Property Relationships of a Biological Mesocrystal in the Adult Sea Urchin Spine. *Proc Natl Acad Sci U A* **2012**, *109*, 3699–3704.
37. Bergström, L.; Sturm (née Rosseeva), E.V.; Salazar-Alvarez, G.; Cölfen, H. Mesocrystals in Biominerals and Colloidal Arrays. *Acc. Chem. Res.* **2015**, *48*, 1391–1402, doi:10.1021/ar500440b.
38. Ma, M.-G.; Cölfen, H. Mesocrystals — Applications and Potential. *Curr. Opin. Colloid Interface Sci.* **2014**, *19*, 56–65, doi:10.1016/j.cocis.2014.03.001.
39. Yin, X.; Griesshaber, E.; Fernández-Díaz, L.; Ziegler, A.; García-García, F.J.; Schmahl, W.W. Influence of Gelatin–Agarose Composites and Mg on Hydrogel-Carbonate Aggregate Formation and Architecture. *Cryst. Growth Des.* **2019**, *19*, 5696–5715, doi:10.1021/acs.cgd.9b00679.
40. Mackenzie, J.K. Second Paper on Statistics Associated with the Random Disorientation of Cubes. *Biometrika* **1958**, *45*, 229–240, doi:10.1093/biomet/45.1-2.229.
41. Hoerl, S.; Griesshaber, E.; Checa, A.G.; Schmahl, W.W. The Biological Crystals in Chamid Bivalve Shells: Diversity in Morphology and Crystal Arrangement Pattern. *Crystals* **2024**, *14*, 649, doi:10.3390/cryst14070649.
42. Ritchie, R.O. Armoured Oyster Shells. *Nat. Mater.* **2014**, *13*, 435–437, doi:10.1038/nmat3956.
43. Gao, H.; Ji, B.; Jäger, I.L.; Arzt, E.; Fratzl, P. Materials Become Insensitive to Flaws at Nanoscale: Lessons from Nature. *Proc. Natl. Acad. Sci.* **2003**, *100*, 5597–5600, doi:10.1073/pnas.0631609100.
44. Gim, J.; Schnitzer, N.; Otter, L.M.; Cui, Y.; Motreuil, S.; Marin, F.; Wolf, S.E.; Jacob, D.E.; Misra, A.; Hovden, R. Nanoscale Deformation Mechanics Reveal Resilience in Nacre of *Pinna Nobilis* Shell. *Nat. Commun.* **2019**, *10*, 4822, doi:10.1038/s41467-019-12743-z.

45. Wegst, U.G.K.; Bai, H.; Saiz, E.; Tomsia, A.P.; Ritchie, R.O. Bioinspired Structural Materials. *Nat. Mater.* **2015**, *14*, 23–36, doi:10.1038/nmat4089.
46. Lu, K. Stabilizing Nanostructures in Metals Using Grain and Twin Boundary Architectures. *Nat. Rev. Mater.* **2016**, *1*, 1–13, doi:10.1038/natrevmats.2016.19.
47. Sun, J.; Bhushan, B. Hierarchical Structure and Mechanical Properties of Nacre: A Review. *RSC Adv.* **2012**, *2*, 7617–7632, doi:10.1039/C2RA20218B.
48. Harper, E.M.; Checa, A.G. Tightly Shut: Flexible Valve Margins and Microstructural Asymmetry in Pterioid Bivalves. *Mar. Biol.* **2020**, *167*, 78, doi:10.1007/s00227-020-03693-y.
49. Carter, J.G. Chapter 10. Evolutionary Significance of Shell Microstructure in the Palaeotaxodonta, Pteriomorphia and Isofilibranchia (Bivalvia: Mollusca). In *Skeletal Biomineralization, Patterns, Processes and Evolutionary Trends*; Carter, J.G., Ed.; Van Nostrand Reinhold, New York, 1990; Vol. 1, pp. 135–296.
50. Griesshaber, E.; Sancho Vaquer, A.; Checa, A.G.; Salas, C.; Harper, E.M.; Schmahl, W.W. The Texture Motif of Ostreoidea Shell Calcite. *Crystals* 2025, *submitted*.
51. Aylmore, L. a. G.; Quirk, J.P. Swelling of Clay–Water Systems. *Nature* **1959**, *183*, 1752–1753, doi:10.1038/1831752a0.
52. Lutterotti, L. Total Pattern Fitting for the Combined Size–Strain–Stress–Texture Determination in Thin Film Diffraction. *Nucl. Instrum. Methods Phys. Res. Sect. B Beam Interact. Mater. At.* **2010**, *268*, 334–340, doi:10.1016/j.nimb.2009.09.053.
53. Schmahl, W.W.; Sancho Vaquer, A.; Checa, A.; Griesshaber, E. The Very Specific Texture Motif of the Oyster Shell Turbostratic Foliated Microstructure. Ludwig-Maximilians-Universität München, Munich, Germany. 2025, *to be submitted*.
54. Yamaguchi, K. Shell Structure and Behaviour Related to Cementation in Oysters. *Mar. Biol.* **1994**, *118*, 89–100, doi:10.1007/BF00699222.
55. Simonet Roda, M.; Griesshaber, E.; Angiolini, L.; Rollion-Bard, C.; Harper, E.M.; Bitner, M.A.; Milner Garcia, S.; Ye, F.; Henkel, D.; Häussermann, V.; et al. The Architecture of Recent Brachiopod Shells: Diversity of Biocrystal and Biopolymer Assemblages in Rhynchonellide, Terebratulide, Thecideide and Craniide Shells. *Mar. Biol.* **2021**, *169*, 4, doi:10.1007/s00227-021-03962-4.
56. Casella, L.A.; He, S.; Griesshaber, E.; Fernández-Díaz, L.; Greiner, M.; Harper, E.M.; Jackson, D.J.; Ziegler, A.; Mavromatis, V.; Dietzel, M.; et al. Hydrothermal Alteration of Aragonitic Biocarbonates: Assessment of Micro- and Nanostructural Dissolution–Reprecipitation and Constraints of Diagenetic Overprint from Quantitative Statistical Grain-Area Analysis. *Biogeosciences* **2018**, *15*, 7451–7484, doi:10.5194/bg-15-7451-2018.
57. Hoerl, S.; Le Moine, T.; Peter, N.J.; Amini, S.; Griesshaber, E.; Wang, J.; Harper, E.M.; Salas, C.; Checa, A.G.; Schwaiger, R.; et al. Crystal Organisation and Material Properties of *Chama* and *Glycymeris* Myostraca and Shells. *Materialia* **2024**, *36*, 102149, doi:10.1016/j.mtla.2024.102149.
58. Hoerl, S.; Micheletti, C.; Amini, S.; Griesshaber, E.; Peharda, M.; Schmahl, W.W. The Difference in Microstructure, Texture and Mechanical Behaviour between *Glycymeris*, *Chama* and *Placopecten* Myostraca. *Materialia* **2024**.
59. Mackinnon, D.I.; Williams, A. The Formation of Muscle Scars in Articulate Brachiopods. *Philos. Trans. R. Soc. Lond. B Biol. Sci.* **1997**, *280*, 1–27, doi:10.1098/rstb.1977.0098.
60. Hoerl, S.; Griesshaber, E.; Häussermann, V.; Achterhold, C.; Amini, S.; Schmahl, W.W. Calcite Crystal Organization and Architecture of the Muscle Scars, the Myotests of Modern Brachiopod Shells. Ludwig-Maximilians-Universität München, Munich, Germany. 2025, *to be submitted*.
61. Carriker, M.R.; Palmer, R.E. A New Mineralized Layer in the Hinge of the Oyster. *Science* **1979**, *206*, 691–693, doi:10.1126/science.206.4419.691.
62. Douvillé, H. Le Test Des Ostréidés Du Groupe de l'*Ostrea Cochlear* (Genre *Pycnodonta*, F. de W.). *C R Hebdm Séances Acad Sci Paris* **1936**, *203*, 1113–1117.
63. Ranson, G. Les Espèces Actuelles et Fossils Du Genre *Pycnodonta* F. de W.: 1. *Pycnodonta Hyotis* (L.). *Bull Mus Natl Hist Nat Paris* **1941**, *13*, 82–92.
64. Chinzei, K.; Seilacher, A. Remote biomineralization I: fill skeletons in vesicular oyster shells. *Jb Geol Paläontol Abh* **1993**, *190*, 349–361.
65. Vermeij, G.J. The Oyster Enigma Variations: A Hypothesis of Microbial Calcification. *Paleobiology* **2013**, *40*, 1–13, doi:10.1666/13002.

66. Banker, R.; Vermeij, G.J. Oyster Microbial Communities and Implications for Chalky Deposit Formation. *Hydrobiologia* **2018**, *816*, 121–135, doi:10.1007/s10750-018-3569-0.
67. Korringa, P. On the Nature and Function of "Chalky" Deposits in the Shell of *Ostrea Edulis* Linnaeus. *Proc. Calif. Acad. Sci. 4th Ser.* **1951**, *27*, 133--158.
68. Pelseneer, P. Hermaphrodite Oysters. *Nature* **1929**, *124*, 14–14, doi:10.1038/124014c0.
69. Galtsoff, P.S. The American Oyster, *Crassostrea Virginica* (Gmelin). *Chesap. Sci.* **1965**, *6*, 199–199, doi:10.2307/1350854.
70. Margolis, S.V.; Carver, R.E. Microsculpture of Chalky Deposits Found in Shells of the Oyster *Crassostrea Virginica*. *The Nautilus* **1974**, *8*.
71. Ullmann, C.V.; Böhm, F.; Rickaby, R.E.M.; Wiechert, U.; Korte, C. The Giant Pacific Oyster (*Crassostrea Gigas*) as a Modern Analog for Fossil Ostreoids: Isotopic (Ca, O, C) and Elemental (Mg/Ca, Sr/Ca, Mn/Ca) Proxies. *Geochem. Geophys. Geosystems* **2013**, *14*, 4109–4120, doi:10.1002/ggge.20257.
72. de Winter, N.J.; Daemmer, L.K.; Falkenroth, M.; Reichart, G.-J.; Moretti, S.; Martinez-Garcia, A.; Hoeche, N.; Schoene, B.R.; Rodiouchkina, K.; Goderis, S.; et al. Multi-Isotopic and Trace Element Evidence against Different Formation Pathways for Oyster Microstructures. *Geochim. Cosmochim. ACTA* **2021**, *308*, 326–352, doi:10.1016/j.gca.2021.06.012.
73. Simonet Roda, M.; Griesshaber, E.; Angiolini, L.; Harper, D.A.T.; Jansen, U.; Bitner, M.A.; Henkel, D.; Manzanero, E.; Müller, T.; Tomašových, A.; et al. The Evolution of Thecideide Microstructures and Textures: Traced from Triassic to Holocene. *Lethaia* **2021**, *54*, 558–577, doi:10.1111/let.12422.
74. Hahn, Th.; Klapper, H. Twinning of Crystals. In *International Tables for Crystallography, Online MRW*; John Wiley & Sons, Ltd, 2006; pp. 393–448 ISBN 978-0-470-68575-4.
75. Richards, R.P. The Four Twin Laws of Calcite and How to Recognize Them. *Rocks Miner.* **1999**, *75*, 308–317.
76. Yin, X.; Griesshaber, E.; Checa, A.G.; Nindiyasari-Behal, F.; Sánchez-Almazo, I.; Ziegler, A.; Schmahl, W.W. Calcite Crystal Orientation Patterns in the Bilayers of Laminated Shells of Benthic Rotaliid Foraminifera. *J. Struct. Biol.* **2021**, *231*, 107707.
77. Lastam, J.; Griesshaber, E.; Yin, X.; Rupp, U.; Sánchez-Almazo, I.; Heß, M.; Walther, P.; Checa, A.; Schmahl, W.W. Patterns of Crystal Organization and Calcite Twin Formation in Planktonic, Rotaliid, Foraminifera Shells and Spines. *J. Struct. Biol.* **2022**, *215*, 107898, doi:10.1016/j.jsb.2022.107898.
78. Lastam, J.; Griesshaber, E.; Yin, X.; Rupp, U.; Sánchez-Almazo, I.; Heß, M.; Walther, P.; Checa, A.; Schmahl, W.W. The Unique Fibrilar to Platy Nano- and Microstructure of Twinned Rotaliid Foraminiferal Shell Calcite. *Sci. Rep.* **2023**, *13*, 2189, doi:10.1038/s41598-022-25082-9.
79. Pokroy, B.; Kapon, M.; Marin, F.; Adir, N.; Zolotoyabko, E. Protein-Induced, Previously Unidentified Twin Form of Calcite. *Proc. Natl. Acad. Sci.* **2007**, *104*, 7337–7341, doi:10.1073/pnas.0608584104.
80. Schmahl, W.W.; Yin, X.; Lastam, J.; Griesshaber, E.; Hörl, S.; Sancho Vaquer, A. Statistical Analysis of EBSD Data and Geometrical Theory of Classical and Non-Classical Twinning in Foraminiferal Shell Calcite. *Nat. Sci. Rep.* 2024, *submitted*
81. Suzuki, M.; Kim, H.; Mukai, H.; Nagasawa, H.; Kogure, T. Quantitative XRD Analysis of {1 1 0} Twin Density in Biotic Aragonites. *J. Struct. Biol.* **2012**, *180*, 458–468, doi:10.1016/j.jsb.2012.09.004.
82. Kogure, T.; Suzuki, M.; Kim, H.; Mukai, H.; Checa, A.G.; Sasaki, T.; Nagasawa, H. Twin Density of Aragonite in Molluscan Shells Characterized Using X-Ray Diffraction and Transmission Electron Microscopy. *J. Cryst. Growth* **2014**, *397*, 39–46, doi:10.1016/j.jcrysgro.2014.03.029.
83. Mutvei, H. Ultrastructural Characteristics of the Nacre in Some Gastropods. *Zool. Scr.* **1978**, *7*, 287–296, doi:10.1111/j.1463-6409.1978.tb00612.x.
84. Griesshaber, E.; Schmahl, W.W.; Ubhi, H.S.; Huber, J.; Nindiyasari, F.; Maier, B.; Ziegler, A. Homoepitaxial Meso- and Microscale Crystal Co-Orientation and Organic Matrix Network Structure in *Mytilus Edulis* Nacre and Calcite. *Acta Biomater.* **2013**, *9*, 9492–9502, doi:10.1016/j.actbio.2013.07.020.
85. Kobayashi, I.; Akai, J. Twinned Aragonite Crystals Found in the Bivalvian Crossed Lamellar Shell Structure. *J. Geol. Soc. Jpn.* **1994**, *100*, 177–180, doi:10.5575/geosoc.100.177.
86. Almagro, I.; Drzymała, P.; Berent, K.; Sainz-Díaz, C.I.; Willinger, M.G.; Bonarski, J.; Checa, A.G. New Crystallographic Relationships in Biogenic Aragonite: The Crossed-Lamellar Microstructures of Mollusks. *Cryst Growth Des* **2016**, *16*.

 doi:10.20944/preprints202502.0108.v1

87. Crippa, G.; Griesshaber, E.; Checa, A.G.; Harper, E.M.; Simonet Roda, M.; Schmahl, W.W. SEM, EBSD, Laser Confocal Microscopy and FE-SEM Data from Modern *Glycymeris* Shell Layers. *Data Brief* **2020**, *33*, 106547, doi:10.1016/j.dib.2020.106547.
88. Crippa, G.; Griesshaber, E.; Checa, A.G.; Harper, E.M.; Simonet Roda, M.; Schmahl, W.W. Orientation Patterns of Aragonitic Crossed-Lamellar, Fibrous Prismatic and Myostracal Microstructures of Modern *Glycymeris* Shells. *J. Struct. Biol.* **2020**, *212*, 107653, doi:10.1016/j.jsb.2020.107653.